A FULL YEAR'S *CHANDRA* EXPOSURE ON SLOAN DIGITAL SKY SURVEY QUASARS FROM THE *CHANDRA* MULTIWAVELENGTH PROJECT

PAUL J. GREEN[1,8], T. L. ALDCROFT[1], G. T. RICHARDS[2], W. A. BARKHOUSE[3,8], A. CONSTANTIN[1], D. HAGGARD[4], M. KAROVSKA[1],
D.-W. KIM[1], M. KIM[5], A. VIKHLININ[1], S. F. ANDERSON[4], A. MOSSMAN[1], V. KASHYAP[1], A. C. MYERS[6], J. D. SILVERMAN[7],
B. J. WILKES[1], AND H. TANANBAUM[1]

[1] Harvard-Smithsonian Center for Astrophysics, 60 Garden Street, Cambridge, MA 02138, USA; pgreen@cfa.harvard.edu
[2] Department of Physics, Drexel University, 3141 Chestnut Street, Philadelphia, PA 15260, USA
[3] Department of Physics, University of North Dakota, Grand Forks, ND 58202, USA
[4] Department of Astronomy, University of Washington, Seattle, WA, USA
[5] International Center for Astrophysics, Korea Astronomy and Space Science Institute, Daejeon, 305-348, Korea
[6] Department of Astronomy, University of Illinois at Urbana-Champaign, Urbana, IL 61801, USA
[7] Institute for Astronomy, ETH Zürich, 8093 Zürich, Switzerland

ABSTRACT

We study the spectral energy distributions and evolution of a large sample of optically selected quasars from the Sloan Digital Sky Survey that were observed in 323 *Chandra* images analyzed by the *Chandra* Multiwavelength Project. Our highest-confidence matched sample includes 1135 X-ray detected quasars in the redshift range $0.2 < z < 5.4$, representing some 36 Msec of effective exposure. We provide catalogs of QSO properties, and describe our novel method of calculating X-ray flux upper limits and effective sky coverage. Spectroscopic redshifts are available for about 1/3 of the detected sample; elsewhere, redshifts are estimated photometrically. We detect 56 QSOs with redshift $z > 3$, substantially expanding the known sample. We find no evidence for evolution out to $z \sim 5$ for either the X-ray photon index Γ or for the ratio of optical/UV to X-ray flux $\alpha_{\rm ox}$. About 10% of detected QSOs show best-fit intrinsic absorbing columns greater than 10^{22} cm^{-2}, but the fraction might reach $\sim 1/3$ if most nondetections are absorbed. We confirm a significant correlation between $\alpha_{\rm ox}$ and optical luminosity, but it flattens or disappears for fainter ($M_B \gtrsim -23$) active galactic nucleus (AGN) alone. We report significant hardening of Γ both toward higher X-ray luminosity, and for relatively X-ray loud quasars. These trends may represent a relative increase in nonthermal X-ray emission, and our findings thereby strengthen analogies between Galactic black hole binaries and AGN. For uniformly selected subsamples of narrow-line Seyfert 1s and narrow absorption line QSOs, we find no evidence for unusual distributions of either $\alpha_{\rm ox}$ or Γ.

Key words: galaxies: active – quasars: absorption lines – quasars: general – surveys – X-rays: general

Online-only material: color figures, machine-readable tables

1. INTRODUCTION

Interest in the properties of active galaxies and their evolution has recently intensified because of deep connections being revealed between supermassive black holes (SMBHs) and galaxy evolution, such as the relationship between the mass of galaxy spheroids and the SMBHs they host (the $M_{\rm BH}$–σ connection; Ferrarese & Merritt 2000; Gebhardt et al. 2000). A feedback paradigm could account for this correlation, whereby winds from active galactic nuclei (AGNs) moderate the SMBH growth by truncating that of their host galaxies (e.g., Granato et al. 2004). Feedback models may explain the correspondence between the local mass density of SMBHs and the luminosity density produced by high-redshift quasars (Yu & Tremaine 2002; Hopkins et al. 2006) as well as the "cosmic downsizing" (decrease in the space density of luminous AGNs) seen in AGN luminosity functions (Barger et al. 2005; Hasinger 2005; Scannapieco et al. 2005). If quasar activity is induced by massive mergers (e.g., Wyithe & Loeb 2002, 2005), then the jigsaw puzzle now assembling may merge smoothly with cosmological models of hierarchical structure formation.

Many, if not most, of the accreting SMBHs in the universe may be obscured by gas and dust in the circumnuclear region, or in the extended host galaxy. The obscured fraction may depend on both luminosity and redshift (Ueda et al. 2003; Brandt & Hasinger 2005; La Franca et al. 2005), and is indeed likely to evolve on grounds both theoretical (e.g., Hopkins et al. 2006a) and observational (Treister & Urry 2006; Ballantyne et al. 2006). Such evolution seems to be required for AGN populations to compose the observed spectrum of the cosmic X-ray background (CXRB; Gilli et al. 2007). However, a full census of all SMBHs remains observationally challenging, since some are heavily obscured, or accreting at very low rates, below the sensitivity limits of current telescopes even at low redshifts.

AGN unification models explain many of the observed differences in the spectral energy distributions (SEDs) of AGNs as being due to the line-of-sight effects of anisotropic distributions of obscuring material near the SMBH (Antonucci 1993). The intrinsic number ratio of obscured-to-unobscured AGN may evolve, and is almost certainly a function of luminosity. Indeed, the ratio in the Seyfert (low-) luminosity regime is currently estimated to be ~ 4, whereas for the QSO (high-) luminosity regime, it may be closer to unity (Gilli et al. 2007).

Astronomers, like most people, usually look where they can see. Type 1 quasars are the easiest AGNs to find in large numbers via either spectroscopic or color selection because of their broad emission lines (FWHM $\gtrsim 1000$ km s^{-1}) and

generally blue continuum slopes and brighter magnitudes. Most of these show few other signs of obscuration such as infrared excess or weakened X-ray emission. Large samples of Type 1 QSOs—as the brightest high-redshift objects—have served to probe intervening galaxies, clusters, and the intergalactic material (IGM) along the line of sight, right to the epoch of re-ionization. Because observed SEDs are thought to be less affected by obscuration and therefore more representative of intrinsic accretion physics, the evolution of this Type 1 sample is of interest as well.

The SEDs and clustering properties of Type 1 QSOs have been studied in increasing detail, probing farther into the universe and wider across the sky and the electromagnetic spectrum. SEDs including mid-infrared photometry from *Spitzer* were compiled and characterized recently for 259 quasars from the Sloan Digital Sky Survey (SDSS) by Richards et al. (2006b). These studies are most useful for calculating bolometric luminosities and *K*-corrections toward understanding the energetics of the accretion process, and its evolution across cosmic time. Studies that target SDSS QSO pairs with small separations find a significant clustering excess on small scales ($\lesssim 40\,\mathrm{kpc}\,h$) of varying strengths (e.g., Hennawi et al. 2006; Myers et al. 2007, 2008), which could be due to mutual triggering, or might simply result from the locally overdense environments in which quasars form (Hopkins et al. 2008).

Optical luminosity function studies of optically selected quasars (e.g., Richards et al. 2006a, 2005; Croom et al. 2004) date back decades (e.g., Boyle et al. 1988). Accurate luminosity functions are needed to trace the accretion history of SMBHs and to contrast the buildup of SMBHs with the growth of galaxy spheroids. An increasing number of optical surveys not only select AGNs photometrically, but also determine fairly reliable photometric redshifts for them. These samples stand to vastly improve the available statistical reliability and the resolution available in the luminosity/redshift plane.

X-ray observations have been found to efficiently select AGNs of many varieties, and at higher surface densities than ever (Hasinger 2005). Independent of the classical AGN optical emission line criteria, X-rays are a primary signature of accretion onto a massive compact object, and the observed X-ray bandpass corresponds at higher redshifts to rest-frame energies capable of penetrating larger intrinsic columns of gas and dust.[9] Even for Type 1 QSOs, X-ray observations have revealed new connections (e.g., between black holes from 10 to $10^9 M_\odot$; Maccarone et al. 2003; Falcke et al. 2004) and new physical insights such as the possibility of ubiquitous powerful relativistic outflows (Middleton et al. 2007) or of relativistically broadened fluorescent Fe Kα emission (see, e.g., the review articles by Fabian et al. 2000; Reynolds & Nowak 2003). Quasars with broad absorption lines (BAL QSOs) blueward of their UV emission lines turn out to be highly absorbed in X-rays (Green et al. 1995, 2001; Green 1996; Gallagher et al. 2002). Quasars that are radio loud are 2–3 times brighter in X-rays for the same optical magnitude (Zamorani et al. 1981; Worrall et al. 1987; Shen et al. 2006), and also may have harder X-ray spectra (e.g., Shastri et al. 1993, although see Galbiati et al. 2005).

The high sensitivity and spatial resolution of *Chandra* and *XMM-Newton* open other avenues for exploration of quasars and their environments. Clusters of galaxies have been discovered in the vicinity of, or along the sightlines to quasars (Green

et al. 2005; Siemiginowska et al. 2005). Lensed quasars have now been spatially resolved in X-rays, unexpectedly showing significantly different flux ratios than at other wavebands (Green et al. 2002; Blackburne et al. 2006; Lamer et al. 2006).

The expected evolution in the environment, accretion rates, and masses of SMBHs in AGNs should correspond to observable evolution in their SEDs. The two most common X-ray measurements used are the X-ray power-law photon index Γ[10] and the X-ray-to-optical spectral slope, α_{ox}.[11] Many of the apparent correlations have been challenged as being artifacts of selection or the by-products of small, heterogeneous samples, which impede progress in our understanding of quasar physics and evolution.

The archives of current X-ray imaging observatories such as *Chandra* and *XMM-Newton* are growing rapidly, and several large efforts for pipeline processing, source characterization (Ptak & Griffiths 2003; Aldcroft 2006), and catalog generation are underway. The 2*XMM* catalog (Page 2006) is available, and the *Chandra* source catalog[12] is due out in 2008 (Fabbiano et al. 2007).

Serendipitous wide-area surveys with *Chandra* were pioneered by the *Chandra* Multiwavelength Project (ChaMP; Green et al. 2004; Kim et al. 2004) for high Galactic latitude, while ChaMPlane (Grindlay et al. 2005) has studied the stellar content of Galactic plane fields. The ChaMP, described in more detail below, also performs multiwavelength source matching and spectroscopic characterization. These efforts are greatly augmented by large surveys such as the SDSS (York et al. 2000), which will obtain spectroscopy of ~100,000 QSOs (e.g., Schneider et al. 2007), and can additionally facilitate the efficient extrapolation of photometric quasar selection with photometric redshift estimation almost a magnitude fainter, toward a million QSOs (e.g., Richards et al. 2008).

The current paper studies the X-ray and optical properties of the subset of these QSOs imaged in X-rays by *Chandra* as part of the ChaMP (Green et al. 2004).

2. THE QUASAR SAMPLE

2.1. The SDSS Quasar Sample

Most large samples of Type 1 QSOs are based on optically selected quasars confirmed via optical spectroscopy (Boyle et al. 1988; Schneider et al. 1994; Hewett et al. 1995). The largest, most uniform sample of optically selected quasars by far has been compiled from the SDSS. With the completion of the SDSS, we can expect some 100,000 spectroscopically confirmed quasars. The SDSS quasars were originally identified to $i < 19.1$ for spectroscopy by their UV-excess colors, with later expansion for $z > 3$ quasars to $i = 20.2$ using *ugri* color criteria (Richards et al. 2002). The large catalog, the broad-wavelength optical photometry, and subsequent follow-up in other wavebands have meant that research results from the SDSS spectroscopic quasar sample better characterize the breadth of the quasar phenomenon than ever before. However, the limited number of fibers available, fiber placement conflicts, and above all the bright magnitude limits of SDSS fiber spectroscopy mean

---

[9] The observed-frame, effective absorbing column is $N_{\mathrm{H}}^{\mathrm{eff}} \sim N_{\mathrm{H}}/(1+z)^{2.6}$ (Wilman & Fabian 1999).

---

[10] Γ is the photon number index of an assumed power-law continuum such that $N_E(E) = N_{E_0} E^{\Gamma}$. In terms of a spectral index α from $f_\nu = f_{\nu_0} \nu^\alpha$, we define $\Gamma = (1 - \alpha)$.

[11] α_{ox} is the slope of a hypothetical power law from 2500 Å to 2 keV; $\alpha_{\mathrm{ox}} = 0.3838 \log(l_{2500\text{Å}}/l_{2\,\mathrm{keV}})$.

[12] The *Chandra* source catalog Web page is http://cxc.harvard.edu/csc.

that 10 times as many quasars have been imaged, and could be efficiently identified from existing SDSS photometry.

Using large spectroscopic AGN samples as "training sets" can produce photometric classification and redshifts of far greater completeness and depth than spectroscopy. Without spectroscopic confirmation, photometric selection criteria strike a quantifiable balance between completeness and efficiency, i.e., a probability can be assigned both to the classification and the redshift. Deep photometric redshift surveys like COMBO-17 (Wolf et al. 2003) have found AGNs to $R = 24$ and $z = 5$ with high completeness. Efficient photometric selection of quasars in the SDSS using a nonparametric Bayesian classification based on kernel density estimation is described in Richards et al. (2004) for SDSS point sources with $i < 21$. An empirical algorithm to determine photometric redshifts for such quasars is described in Weinstein et al. (2004). The spectroscopic training samples for these methods now include far more high-redshift quasars, and so the algorithms have been retrained to include objects redder than $(u - g) = 1.0$ to classify high-z quasars, and applied to the much larger SDSS Data Release 6 (DR6). This large catalog of ~ 1 million photometrically identified QSOs and their photometric redshifts is described in Richards et al. (2008). They estimate the overall efficiency of the catalog to be better than 72%, with subsamples (e.g., X-ray detected objects) being as efficient as 97%. These estimates are based on an analysis of the autoclustering of the objects in the catalog (Myers et al. 2006), which is very sensitive to stellar interlopers. However, at the faint limit of the catalog some additional galaxy contamination is expected.

For luminosity and distance calculations, we adopt an $H_0 = 70$ km s^{-1} Mpc^{-1}, $\Omega_\Lambda = 0.7$, and $\Omega_M = 0.3$ cosmology throughout. We assume $\alpha = -0.5$ for the optical continuum power-law slope ($v \propto \nu^\alpha$, where ν is the emission frequency), and derive the rest-frame, monochromatic optical luminosity at 2500 Å ($l_{2500Å}$; units erg s^{-1}Hz^{-1}) using the SDSS dereddened magnitude with central wavelength closest to $(1 + z) \times 2500$ Å.

2.2. The Extended Chandra Multiwavelength Project

The ChaMP is a wide-area serendipitous X-ray survey based on archival X-ray images of the ($|b| > 20$ deg) sky observed with the AXAF CCD Imaging Spectrometer (ACIS) onboard *Chandra*. The full 130-field Cycle 1–2 X-ray catalog is public (Kim et al. 2007b), and the most comprehensive X-ray number counts (log N–log S) to date have been produced thanks to 6600 sources and massive source-retrieval simulations (Kim et al. 2007a). We have also published early results of our deep ($r \sim 25$) NOAO/MOSAIC optical imaging campaign (Green et al. 2004), now extended to 67 fields (W. A. Barkhouse et al. 2009, in preparation). ChaMP results and data can be found online.[13]

To improve statistics and encompass a wider range of source types, we have recently expanded our X-ray analysis to cover a total of 392 fields through *Chandra* Cycle 6. We chose only fields overlapping with SDSS DR5 imaging. To ease analysis and minimize bookkeeping problems, the new list of *Chandra* pointings (observation IDs; "obsids" hereafter) avoids any overlapping observations by eliminating the observation with the shorter exposure time. As described in Green et al. (2004), we also avoid fields with large ($\gtrsim 3'$) extended sources in either optical or X-rays (e.g., nearby galaxies M101, NGC 4725, NGC 4457, or clusters of galaxies MKW8, or Abell 1240). Spurious X-ray sources (due to, e.g., hot pixel, bad bias, bright

---
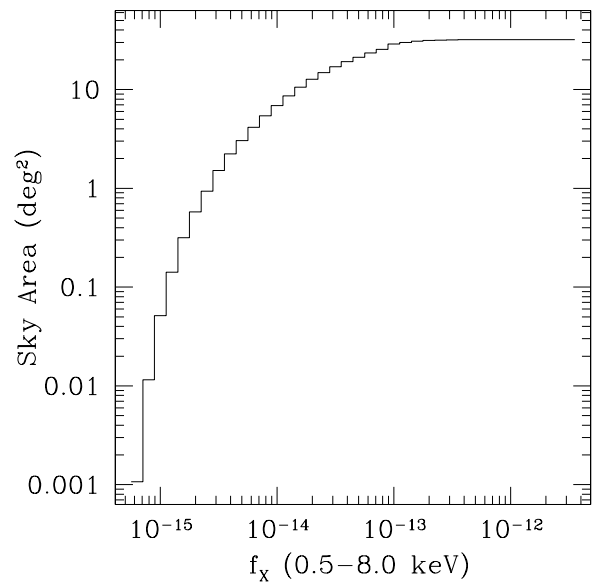
Figure 1. Sky area vs. *B*-band (0.5–8 keV) flux limit for the 323 obsids included in our ChaMP/SDSS field sample. Flux limit is defined here as the number of counts detectable in 90% of simulation trials, converted to flux assuming a power-law $\Gamma = 1.7$ at $z = 0$ and the Galactic N_H appropriate to each obsid. Chip S4 (CCD ID 8) is excluded throughout. The area covered at the brightest fluxes is 32 deg^2.

source readout streaks) have been flagged and removed as described in Kim et al. (2007b). Of the 392 ChaMP obsids, 323 overlap the SDSS DR5 footprint.

The ChaMP has also developed and implemented an `xskycover` pipeline which creates sensitivity maps for all ChaMP sky regions imaged by ACIS. This allows (1) identification of imaged-but-undetected objects, (2) counts limits for 50% and 90% detection completeness, and (3) corresponding flux upper limits at any sky position, as well as (4) flux sensitivity versus sky coverage for any subset of obsids, as needed for log N–log S and luminosity function calculations. Our method is described in the Appendix, and has been verified recently by Aldcroft et al. (2008) using the *Chandra* Deep Field South (CDF-S). The final sky ChaMP/SDSS coverage area (in deg^2) for the 323 overlapping fields as a function of broadband (*B* band 0.5–8 keV) flux limit is shown in Figure 1 (see caption for specific definition of this limit). The area covered at the brightest fluxes is 32 deg.^{2} On average five CCDs are activated per obsid.

We have downloaded into the ChaMP database all the SDSS photometry, and the list of photo-z quasar candidates within $20'$ of the *Chandra* aim point for each such obsid.[14] Because the *Chandra* point-spread function (PSF) increases with off-axis angle (OAA), comparatively few sources are detected beyond this radius, and source centroids also tend to be highly uncertain. Of X-ray detected candidates, we will show in Section 2.4 that 98% of these candidates with spectra are indeed QSOs.

Next we describe the identification of high-confidence ChaMP X-ray counterparts to SDSS QSOs in Section 2.3. We then discuss in Section 2.4 spectroscopic identifications for these objects. Section 3 then describes results for several interesting QSO subsamples, including our treatment of SDSS quasars that were not X-ray detected.
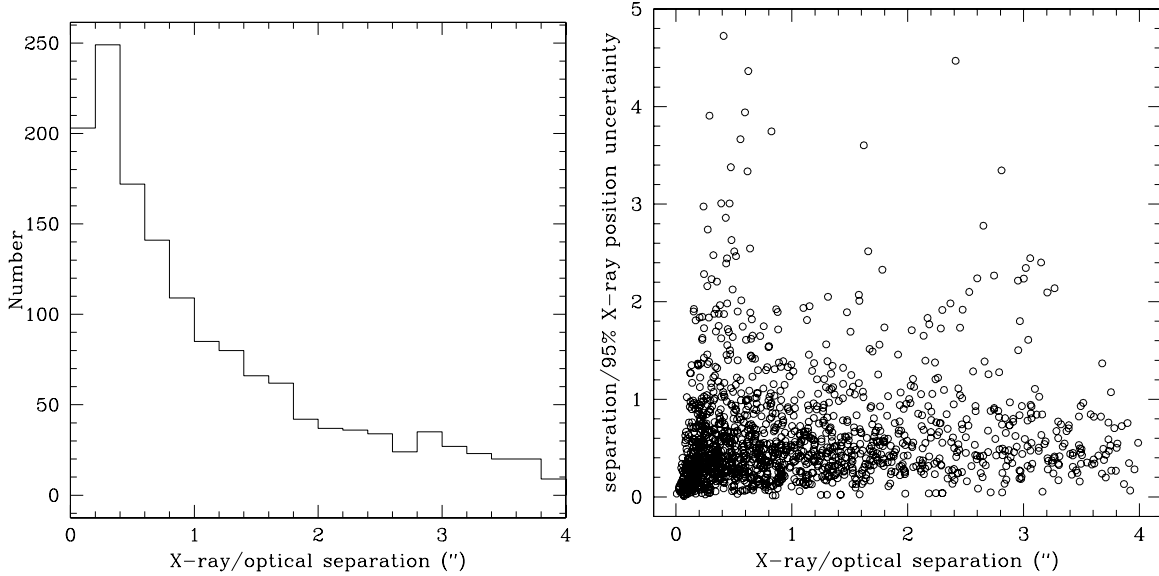
Figure 2. Positional offsets of matched sample. Left: the histogram of X-ray/optical centroid separations in the full matched sample of 1376. The mode is $0\rlap{.}''3$, the median is $0\rlap{.}''76$, and the mean is $1\rlap{.}''1$. Right: the ratio of the X-ray/optical centroid separation to the 95% X-ray positional uncertainty vs. separation. The fraction of objects with separations larger than the 95% uncertainty (i.e., with ratio greater than 1) remains relatively constant, and virtually no separations wider than $3''$ are larger than the positional uncertainty σ_{XP95}.

2.3. X-Ray/Optical Matching

The positional uncertainty of ChaMP X-ray source centroids has been carefully analyzed via X-ray simulations by Kim et al. (2007a) and depends strongly on both the number of source counts and the OAA. Cross-correlating ChaMP X-ray source centroids with QSOs, we find that 95% of the X-ray/optical separations d_{XO} of matched QSOs are smaller than the 95% X-ray positional uncertainty σ_{XP95}. We first perform an automated matching procedure between each optical QSO position and the ChaMP's X-ray source catalog. We adopt $4''$ as our matching radius criterion. Figure 2 shows that 95% of the matched sample has an X-ray/optical position difference of less than $3''$, and expansion to include match radii above $4''$ would not substantially increase the sample size. Searching the ChaMP catalog for X-ray sources within $4''$ of the optical SDSS quasar coordinate, yields 1376 unique matches in the "Matched" sample.

Although the overall efficiency of the SDSS photometric QSO catalog is only expected to be 72% (Richards et al. 2008), the rarity of luminous Type 1 quasars and X-ray sources means that matched objects should be quite clean. By repeatedly offsetting the SDSS coordinates of each QSO by $36''$ and rematching to the ChaMP X-ray catalog, we derive a spurious match rate of just 0.7%.[15] This excellent result is due to *Chandra*'s $\sim$ arcsec spatial resolution, which at SDSS depths allows for unambiguous counterpart identification, given that both Type 1 QSOs and X-ray sources are relatively sparse on the sky.

We identify and remove a variety of objects with potentially poor data, including overlapping multiple sources (some of which are targeted lenses), bright X-ray sources suffering from pile-up, optical sources with photometry contaminated by close brighter sources or within large extended galaxies, or stellar diffraction spikes.

In addition to the automated matching procedure, we also perform visual inspection (VI) of both X-ray and optical images, overplotting the centroids and their associated position errors. We retain only the highest-confidence matches (matchconf=3). Most of the 105 objects we thereby eliminate have large ratios of d_{XO}/σ_{XP95}, or multiple candidate optical counterparts. We note that some of the most interesting celestial systems may be found among sources with matchconf<3. For example, these might include QSOs that are lensed, have bright jets, or are associated with host or foreground optical clusters or galaxies. Systems that are poorly matched, multiply matched, or photometrically contaminated may account for up to $\sim$10% of the full X-ray-selected sample. We therefore caution against blind cross-correlation of large source catalogs (e.g., the *Chandra* Source Catalog)[16] without such detailed quality control and visual examination of images. However, since we seek here to analyze the multiwavelength properties of a large clean sample of QSOs, and since most of these more complicated systems require significant further analysis or observation, we defer their consideration to future studies.

2.4. Spectroscopic Redshift Information

After cross-correlation with the X-ray catalog, we sought spectroscopic redshifts for any objects in the photometric QSO catalog. For this purpose, we obtained redshifts from existing ChaMP spectroscopy, from the SDSS (DR6) database itself, and then finally we searched the literature by cross-correlating optical positions with the NASA Extragalactic Database (NED), using a $2''$ match radius. Of 1376 matched objects, we found high confidence spectroscopic redshifts for 407, of which 43 spectra were observed by the ChaMP. In striking testimony to the quality of the quasar selection algorithm (especially once candidates have been matched to X-ray sources) only eight of these (2%) are not broad-line AGNs. Three are narrow emission line galaxies, two are absorption line galaxies (no emission lines of equivalent width $W_\lambda > 5$ Å), and three are known BL Lac objects. We exclude these objects from all samples described below. Because

---

[15] The ratio of the number of X-ray matches to the optical control sample to the number of matches in the actual sample is 0.0067.

[16] The *Chandra* Source Catalog, available at http://cxc.cfa.harvard.edu/csc, contains all X-ray sources detected by the *Chandra* X-ray Observatory.
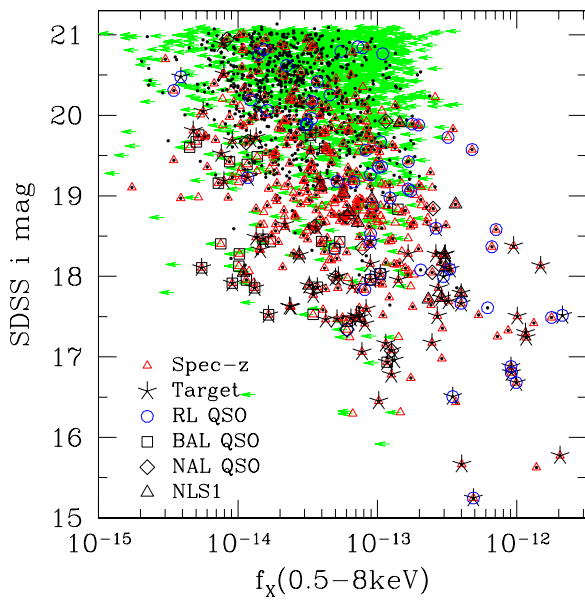
Figure 3. SDSS *i* magnitude vs. broadband (0.5–8 keV) X-ray flux for the SDSS/ChaMP QSO the Main sample. The flux shown is based on the best-fit PL-free `yaxx` model, with the effect of Galactic absorption removed from both X-ray and optical. X-ray detections are marked by black dots and flux upper limits by green arrows. The open red triangles show QSOs with existing spectroscopic redshifts, clearly biased toward brighter optical mags. Radio-loud quasars (large open blue circles), BAL QSOs (open black squares), NAL QSOs (open black diamonds) and NLS1s (open black triangles), and *Chandra* PI targets (large asterisks) are also indicated as shown in the legend.

(A color version of this figure is available in the online journal.)

the magnitude distribution (and therefore the photometric color errors) for objects lacking spectroscopic classifications is fainter (see Figure 3), we expect that the overall fraction of misclassified photo-*z* QSOs is larger than 2%, but it would be difficult to estimate it without deeper spectroscopic samples. A plot of the photometric versus spectroscopic redshifts of these quasars is shown in Figure 4.

3. SAMPLES, SUBSAMPLES, AND DETECTION FRACTIONS

The definition of our Main sample and a variety of subsamples are described in subsequent sections and summarized in Table 1. The size of our Main sample allows us to investigate the effects of luminosity or redshift limits, X-ray nondetections, PI target bias, strong radio-related emission (RL QSOs), broad- and narrow-line absorption (BAL and NAL, respectively, QSOs), and Narrow-Line Seyfert 1s (NLS1s). In Table 1, samples to which we refer frequently are arrayed under "Primary Samples" in decreasing order of the number of detections. Samples mentioned only once or twice in this paper are listed in similar order under "Other Samples." Tables listing bivariate statistical results (Tables 5–7) later in the paper list samples in this same order for reference.

We define the Main sample to be the 2308 SDSS QSOs that fall on *Chandra* ACIS chips in a region of effective exposure greater than 1200 s (excluding CCD 8; see below), regardless of *Chandra* X-ray detection status. Our cleaned matched sample (the MainDet sample) of X-ray/optical matched QSOs contains 1135 distinct X-ray sources with high optical counterpart match confidence, where we have removed all sources (1) with significant contamination by nearby bright optical sources, (2) with significant overlap with other X-ray sources, (3) with detected

on ACIS-S chip S4 (`CCD` 8), because of its high background and streaking, (4) with dithering across chips (which renders unreliable the `yaxx` X-ray spectral fitting described below), or (5) with spectroscopy indicating that the object is not a Type 1 QSO.

The mean exposure time for the MainDet sample is 25.9 ks per QSO, with an average of 3.6 QSOs detected on each *Chandra* field.[17] For the 1173 nondetections in the Main sample, the mean exposure time is 17.6 ks. A histogram of exposure times for all QSOs in the Main sample is shown in Figure 5.

We publish key data for 1135 QSOs in the MainDet sample in Table 2, marking 82 sources that are the intended *Chandra* principal investigator (PI) targets. X-ray sources in plots include only the MainDet sample or subsets of it. Figure 6 shows luminosity versus redshift for the MainDet sample. A large fraction of the $z > 4$ objects are *Chandra* targets (large black stars). Strong redshift–luminosity trends are seen both in optical and X-ray, as is expected from any flux-limited survey. However, the factor ~30–50 range in luminosity is unusual for a single sample; such breadth is usually only achieved using sample compilations encompassing diverse selection techniques. In Figure 6, the large number of objects in our sample makes it difficult to distinguish the point-types presenting object class information, so Figure 7 shows a zoom-in on the most densely populated regions of the *L–z* plane.

Since we start with Type 1 SDSS QSOs, we are studying an optically selected sample, and the selection function is complex (Richards et al. 2006a). If we limit the analysis to detections only, then the sample is both optically and X-ray selected, and the selection function becomes increasingly complex. If instead we include all X-ray upper limits in the analysis, the sample remains fundamentally optically selected, but then statistical analyses must incorporate the nondetections (see Section 6.1).

The ChaMP's `xskycover` pipeline allows us to investigate the detection fraction for the full SDSS QSO sample, shown in Figure 8. Of 2308 SDSS QSOs that fall on an ACIS chip (the Main sample) in our 323 ChaMP fields, 1135 (49%) are detected in the MainDet sample. Detection fractions as a function of SDSS QSO mag and redshift for this sample are shown in Figure 9. To minimize sample biases, we can also examine detection fractions as a function of X-ray observing parameters like exposure time and OAA. To simultaneously optimize detected sample size and detection fraction, we simply maximize $N_{\mathrm{det}}^2/N_{\mathrm{lim}}$, where N_{det} and N_{lim} are the number of X-ray detections and nondetections (flux upper limits), respectively. We find that an X-ray-unbiased subsample with a significantly higher detection rate is achieved by limiting consideration to the 1269 QSOs with OAA $< 12'$ and exposure time $T > 4$ ks, of which 922 (72%) are detections. This high detection fraction sample is called the D2L sample (Table 1).

Data for X-ray nondetections is available in Table 3. We include in Table 3 only the 347 limits in the D2L sample, where the flux limits are sensitive enough to be interesting. By "interesting," we mean that the limits are close to or brighter than the faint envelope of detections. A flux limit several times brighter than that envelope provides no statistical constraints whatsoever on the derived distributions or regressions. For X-ray nondetections, data are more sparse all around for several reasons. QSOs with limits are optically fainter (mean and median $i = 20.4$ mag for the D2L sample limits compared to $i = 19.9$

---

[17] For 14 of 323 *Chandra* fields, no QSOs are detected.
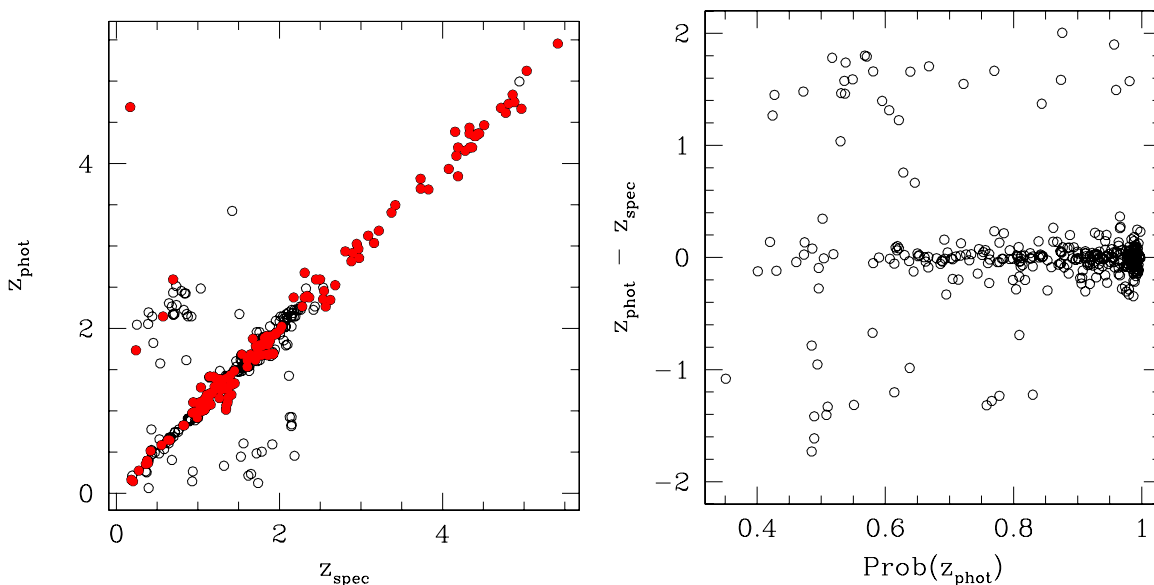
Figure 4. Left: photometric redshift vs. spectroscopic redshift for QSOs detected in ChaMP fields. Filled (red) circles show QSOs for which the formal photometric redshift probability is greater than 95%. A fraction of objects have large errors in their photometric redshifts. About 18% of QSOs with $z_{spec} < 1$ have $z_{phot} > 2$. This drops to 13% using only Prob(z_{phot}) > 0.5. Right: difference between the photometric and true (spectroscopic) redshift for QSOs in our sample, plotted against photometric redshift probability, again illustrates the reliability of these probabilities.

(A color version of this figure is available in the online journal.)
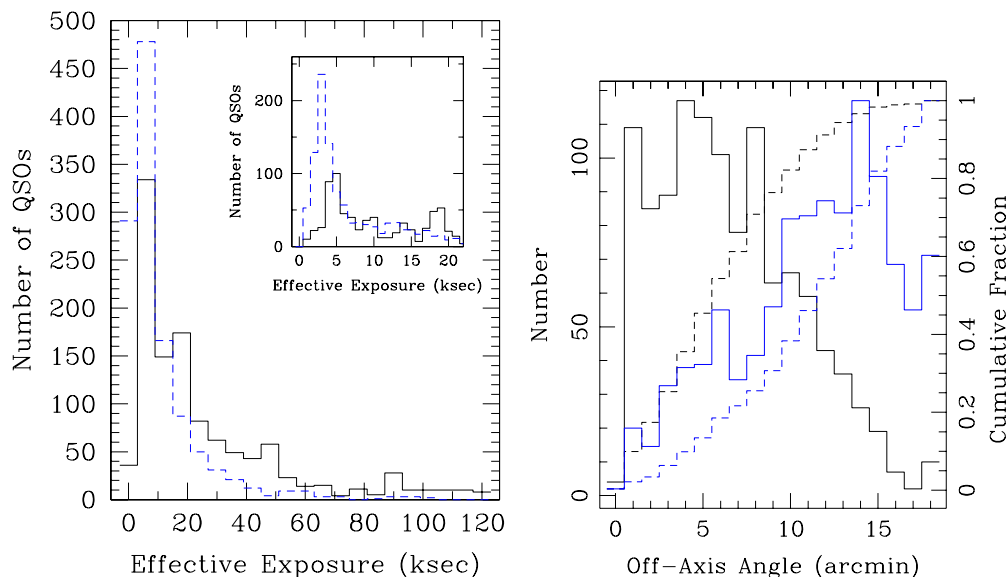
Figure 5. Left: histogram of effective *Chandra* exposure times for QSOs in the Main sample, in units of ks, with bin size 6 ks for detections (solid black line) and limits (dashed blue line). For detections, the mean and median exposure times are 25.9 and 17.6 ks, respectively. The inset shows detail at low exposure times using bin size 1 ks. Right: histogram of *Chandra* OAAs for the Main sample, in units of arcmin. The black solid histogram shows how detections trend toward small OAA. Mean and median for detections are $6\farcm4$ and $5\farcm8$, respectively. Blue histogram shows that limits trend toward large OAA. The dashed histograms show the corresponding cumulative fractions. About 90% of the detections (compared to ∼ 50% of the limits) are at OAA < 12′ off-axis.

(A color version of this figure is available in the online journal.)

for detections). Being fainter, fewer have SDSS spectroscopy. Also, as nondetections, none have been targeted for spectra by the ChaMP, so globally only about 10% of nondetected QSOs have optical spectra. The fraction of radio detections is also smaller (1.2% versus 4.8%). None are *Chandra* PI targets. Finally, X-ray nondetections lacking optical spectroscopy are somewhat less likely to be QSOs. The selection efficiency (fraction of QSO candidates that are actual QSOs) between about $0.8 < z < 2.4$ is ∼95% (Richards et al. 2004; Myers et al. 2006), but Richards et al. (2008) estimate that near the faint

limit of $i \sim 20.4$ mag, the overall QSO selection efficiency is ∼80%. Particular attention must be paid to possible galaxy contamination at the faint end as the autoclustering estimates of the efficiency do not include galaxy interlopers at faint limits where SDSS star–galaxy separation begins to break down. However, many of these "spurious" cross-matches may turn out to be (e.g., low-luminosity) AGNs. In any case, the increased level of contamination by non-QSOs is another rationale for limiting the number of nondetections to those with sensitive X-ray limits. The nature of the statistical analysis (as discussed

Table 1
Quasar Sample Definitions

Sample	Lims[a]	Targets	RL	Abs[b]	T_{min}	OAA	N_{det}	N_{lim}	N_{total}	% Det
				Primary Samples						
Main	y	...	...	...	...	...	1135	1173	2308	49
MainDet	...	...	...	...	...	...	1135	0	1135	100
noTDet	...	n	...	...	...	...	1053	0	1053	100
D2L	y	...	...	...	4	12	922	347	1269	72
D2LNoRB	y	...	n	n	4	12	866	338	1204	71
hiLo	y	...	n	n	...	...	847	961	1808	46
HiCtNoTRB	...	n	n	...	...	...	129	0	129	100
				Other Samples						
NoRB	y	...	n	n	...	...	1054	1144	2198	47
NoRBDet	...	...	n	n	...	...	1054	0	1054	100
D2LNoTRB	y	n	n	n	4	12	828	338	1166	71
hiLoLx	...	...	n	n	...	...	801	0	801	100
zLxBox	...	...	...	...	...	...	817	0	817	100
LoBox	...	...	...	...	...	...	530	0	530	100
zBox	y	...	...	...	...	...	420	360	780	53
zBoxDet	...	...	...	...	...	...	420	0	420	100
D2LSy1	y	...	n	n	...	...	176	84	260	68
HiCt	...	...	...	...	...	...	157	0	157	100
HiCtNoTRB	...	n	n	n	...	...	129	0	129	100

Notes.
[a] If "y," sample includes X-ray nondetections.
[b] If "n," sample excludes QSOs with evident BALs or NALs and also NLS1s.

in Section 6.1) is such that nondetections are included, but are assumed to follow the distribution of detections, and so effectively have a lower weight in the results.

Amongst the undetected QSOs in the Main sample, 165 have SDSS spectroscopy, of which 144 are high confidence spectroscopic QSOs. The 21 non-QSOs comprise 16 stars and five galaxies. The higher (13%) rate of nonstar spectroscopic classifications amongst undetected QSOs is not surprising, since X-ray detection greatly increases the probability that an optical AGN candidate is indeed an AGN. From the upper limit QSO sample, we remove the 22 non-QSOs, and use the SDSS spectroscopic redshifts instead of the photometric redshifts wherever applicable.

3.1. Targets

The "Nontarget" detected sample (the noTDet sample) of 1053 QSOs further eliminates 82 objects (7.2% of the MainDet sample) that are the intended targets of the *Chandra* observation wherein they are found. Targets are on average brighter than most of the QSO sample (see Figure 3), but more importantly were chosen for observation for a variety of reasons unrelated to this study. In particular, targets tend to be more luminous than serendipitous QSOs (Figures 6 and 7), and several are known lenses (e.g., HS 0818+1227, PG 1115+080, UM 425 = QSO 1120+019). The bias in sample characteristics is largely mitigated in the subsamples excluding targets (see Table 1). However, the exclusion of targets also produces a (much smaller) bias because some objects with similar characteristics would have been included (at a lower rate) were the *Chandra* pointings all truly random. Because many of the targets are indeed of interest (e.g., high-z QSOs), we include them in most discussions, but always check that results are consistent without them. We also note that some target bias probably affects the X-ray sample even after the exclusion of PI target QSOs, because PI targets may cluster with other categories of X-ray sources such as other AGN, galaxies, or clusters. Overall,

a comparison of regression results[18] for several of our subsamples that differ only in target exclusion does not indicate a significant target bias, due at least in part to our large sample sizes.

3.2. Radio Loudness

Quasars with strong radio emission are observed to be more X-ray luminous (e.g., Green et al. 1995; Shen et al. 2006). At least some of the additional X-ray luminosity is likely to originate in physical processes related to the radio jet rather than to the accretion disk, so it may be important to recognize those objects that are particularly radio loud.

The *Faint Images of the Radio Sky at Twenty Centimeters* (*FIRST*) survey (Becker et al. 1995) from the NRAO Very Large Array (VLA) has a typical (5σ) sensitivity of $\sim$1 mJy, and covers most of the SDSS footprint on the sky. Following Ivezić et al. (2002), we adopt a positional matching radius of 1".5, which should result in about 85% completeness for core-dominated sources, with a contamination of $\sim$3%. We thereby match 69 sources to the Matched sample. Jiang et al. (2007) matched the *FIRST* to SDSS spectroscopic quasars and found that about 6% matched within 5". We might expect a lower matched fraction because our optical photometric sample extends 1–2 mag fainter. On the other hand, we are looking at X-ray-detected quasars, so the actual matched fraction of $\sim$5% is similar. We also matched all the quasar optical positions to the *FIRST* within 30", and visually examined all the *FIRST* images to look for multiple matches and/or lobe-dominated quasars. There are 26 sources that we judged to have reliable morphological complexity that are resolved by *FIRST* into multiple sources. The NRAO VLA Sky Survey (NVSS; Condon et al. 1998), lists detections for 19 of these. Comparing NVSS with summed *FIRST* fluxes, we found NVSS fluxes slightly larger: less 2% difference in the mean ($\sim$20% max). Since the NVSS beam is larger (45") than

---

[18] Table 6 and 7 shows similar results comparing, e.g., the MainDet sample and the noTDet sample, or the D2LNoRB sample and the D2LNoTRB sample.

Table 2
Properties of SDSS Quasars Detected by *Chandra*

SDSS Obj ID (1)	R.A. (J2000) (2)	Decl. (3)	i (4)	z_{phot} (5)	P_z (6)	z_{lo} (7)	z_{hi} (8)	z_{best} (9)	Spec Ref (10)	CXOMP (11)	srcid (12)	OAA (13)	cts (14)	cts_err (15)	Exposure (16)	N_H^{Gal} (17)
587731187277889693	0.50832	0.761275	19.043	1.395	0.962	0.980	1.550	1.3950		J000202.0+004541	XS04861B2_001	8.2	41.2	7.6	5.6	2.5
587731187277955083	0.62797	0.833065	17.955	1.275	0.973	1.030	1.480	1.3527	S	J000230.7+004959	XS04861B7_001	0.6	132.7	12.7	5.0	2.5
588015510343385196	0.64800	0.889224	20.249	1.895	0.841	1.410	2.140	1.895		J000235.5+005321	XS04861B7_008	4.1	7.5	3.8	5.0	2.5
587731186204606566	1.59420	−0.073452	19.575	1.285	0.993	1.010	1.440	1.0370	R	J000622.6-000424	XS04096B5_002	13.1	217.3	16.6	4.2	3.0
587731186204606704	1.64276	−0.085489	20.770	1.605	0.450	1.440	2.000	1.6050		J000634.3-000510	XS04096B5_001	10.9	42.8	8.9	4.2	3.0
588015508733231171	1.72545	−0.259281	17.878	1.675	0.919	1.440	2.080	1.7195	R	J000654.1-001533	XS04096B7_001	0.6	41.7	7.5	4.2	3.0
588015508733231262	1.72868	−0.230998	20.345	2.485	0.552	2.110	2.670	2.4850		J000654.9-001351	XS04096B7_003	1.2	8.6	4.1	4.2	3.0
588015508733231265	1.74704	−0.294690	19.428	1.975	0.857	1.600	2.180	1.9750		J000659.2-001740	XS04096B7_002	3.0	22.8	5.9	4.2	3.0
587731186204737774	1.82682	−0.088692	20.734	1.205	0.811	0.900	1.520	1.2050		J000718.5-000522	XS04096B2_002	11.5	13.6	5.3	3.6	3.0
587730773889974538	2.81349	14.767168	18.276	4.665	0.976	4.490	5.070	4.9672	S	J001115.2+144601	XS03957B7_001	0.6	129.8	12.5	3.4	9.6
587731186742198291	3.19633	0.210979	18.970	2.145	0.703	1.880	2.240	2.1528	S	J001247.0+001241	XS04829B6_007	8.9	10.9	4.7	6.6	5.6
588015509270822924	3.27563	0.075532	18.463	0.815	0.510	0.670	0.970	2.1453	R	J001306.1+000431	XS04829B7_005	0.6	15.6	5.1	6.6	5.6
588015509270823186	3.30851	0.053632	20.625	2.055	0.539	1.430	2.300	2.0550		J001314.0+000313	XS04829B7_001	2.8	40.6	7.5	6.6	5.6
588290881639350481	5.07661	15.715105	20.375	0.885	0.538	0.640	1.200	0.8850		J002018.3+154254	XS01595B7_004	1.6	4.5	3.4	13.3	4.2
588290881639350569	5.08519	15.735262	20.942	2.175	0.608	1.430	2.360	2.1750		J002020.4+154406	XS01595B6_001	2.1	15.6	5.1	16.6	4.2
587730775501504810	5.08732	15.914392	21.076	0.175	0.958	0.060	0.240	0.1750		J002020.7+155451	XS01595B5_004	12.7	44.9	10.9	12.7	4.2
588290881639350397	5.10509	15.681860	17.173	1.985	0.921	1.440	2.160	2.0091	S	J002025.2+154054	XS01595B7_001	1.3	494.3	23.4	13.3	4.2
588015507661324390	5.82850	−1.050280	19.666	1.215	0.990	0.980	1.450	1.2150		J002318.8-010301	XS04079B7_001	1.7	23.9	6.0	1.6	21.2
588015509809266720	6.96833	0.437687	17.733	0.145	0.933	0.140	0.240	0.2053	S	J002752.4+002615	XS04080B7_003	4.5	39.2	7.6	1.5	44.9
588015509809659937	7.88101	0.572282	18.474	1.875	0.868	1.620	2.040	1.7354	S	J003131.4+003420	XS02101B7_002	1.2	28.8	6.5	3.8	2.4
587727227305066749	10.07393	−9.190477	20.752	0.145	0.649	0.100	0.250	0.1450		J004017.7-091125	XS04888B3_010	7.6	19.8	5.8	8.8	3.4
587727227305197873	10.30287	−9.238581	20.770	1.295	0.635	1.000	1.570	1.2950		J004112.6-091417	XS04888B1_010	11.0	16.1	6.5	8.6	3.4
587731185135648990	12.47624	−0.939257	20.389	2.145	0.702	1.440	2.260	2.1450		J004954.3-005620	XS04825B7_018	4.7	10.8	4.4	12.9	2.1
587731185135648996	12.48751	−0.968442	20.758	0.385	0.551	0.250	0.500	0.3850		J004957.0-005806	XS04825B7_012	5.8	26.9	6.6	12.9	2.1
588015508201144501	12.62757	−0.780014	20.845	1.265	0.961	0.900	1.470	1.2650		J005030.6-004649	XS04825B2_003	8.5	21.9	6.2	12.3	2.1
588015508201144513	12.65482	−0.808028	20.411	1.855	0.883	1.620	2.110	1.8550		J005037.2-004829	XS04825B2_001	8.8	23.8	6.2	12.3	2.1
587731186209783863	13.47981	−0.052600	17.984	0.485	0.778	0.390	0.700	1.7189	S	J005355.1-000309	XS04830B7_001	0.6	27.7	6.4	7.0	1.9
588015509275803698	14.77296	0.114358	17.489	0.745	0.842	0.660	0.950	0.7189	S	J005905.4+000651	XS02179B6_001	5.5	324.7	19.6	2.2	3.0
588015509275869378	14.84438	0.050395	19.194	4.385	0.998	4.200	4.560	4.1544	S	J005922.6+000301	XS02179B7_003	0.6	10.8	4.4	2.6	3.0

Table 2
(Continued.)

| SDSS Obj ID (1)	$N_H^{\rm intr}$ (18)	$N_H^{\rm hi}$ (19)	$N_H^{\rm lo}$ (20)	Γ (21)	$\Gamma^{\rm hi}$ (22)	$\Gamma^{\rm lo}$ (23)	$\log f_x$ (24)	$\log l_{2\,{\rm keV}}$ (25)	$\log l_{2500\,{\rm \AA}}$ (26)	$\alpha_{\rm ox}$ (27)	$f_{20\,{\rm cm}}$ (28)	Ext (29)	R (20)	Class (31)	Targ (32)	Comments (33)
587731187277889693				1.53	0.45	−0.44	−12.960	26.988	30.590	1.383		0	1.06	0	0	
587731187277955083				2.40	0.42	−0.38	−12.850	27.065	30.978	1.502		0	0.62	0	1	
588015510343385196				2.14	1.25	−1.03	−13.990	26.286	30.391	1.576		0	1.54	0	0	
587731186204606566	0.00	0.27	0.00	1.74	0.30	−0.24	−12.321	27.308	30.020	1.041	3897.60	1	4.86	0	0	NED: FBQS J0006-0004
587731186204606704				1.31	0.49	−0.46	−12.870	27.228	29.899	1.025		0	1.75	0	0	
588015508733231171				2.05	0.46	−0.44	−13.180	26.992	31.173	1.605		0	0.59	0	1	NED: LBQS 0004-0032
588015508733231262				3.50	1.87	−1.26	−14.000	26.563	30.650	1.569		0	1.58	0	0	
588015508733231265				2.27	0.68	−0.62	−13.470	26.850	30.758	1.500		0	1.21	0	0	
587731186204737774				1.82	0.91	−0.79	−13.230	26.561	29.765	1.230		0	1.73	0	0	
587730773889974538				1.88	0.37	−0.35	−12.580	28.701	32.063	1.290		0	0.75	0	1	
587731186742198291				2.13	1.02	−0.89	−13.730	26.681	31.020	1.666		0	1.03	0	0	
588015509270822924				2.10	0.87	−0.74	−13.820	26.587	31.220	1.778		0	0.82	1	1	HiBAL NED: LBQS 0010-0012
588015509270823186				1.47	0.43	−0.41	−13.220	27.142	30.316	1.218		0	1.69	0	0	
588290881639350481				2.05	1.48	−1.24	−14.640	24.819	29.639	1.850		0	1.59	0	0	
588290881639350569				1.72	0.73	−0.67	−14.010	26.412	30.241	1.470		0	1.82	0	0	
587730775501504810				1.69	0.70	−0.63	−13.450	24.354	27.578	1.238		0	1.87	0	0	
588290881639350397	0.00	0.47	0.00	1.77	0.16	−0.12	−12.609	27.729	31.676	1.515		0	0.31	0	1	
588015507661324390				1.94	0.60	−0.57	−13.000	26.799	30.231	1.317		0	1.31	0	0	
588015509809266720				1.28	0.50	−0.46	−12.540	25.418	29.033	1.388		0	0.53	3	1	NLSy1
588015509809659937				2.23	0.58	−0.54	−13.360	26.822	30.939	1.581		0	0.83	0	0	
587727227305066749				1.91	0.73	−0.67	−13.540	24.084	27.718	1.395		0	1.74	0	0	
587727227305197873				1.16	0.79	−0.73	−13.410	26.458	29.783	1.276		0	1.75	0	0	
587731185135648990				0.95	0.89	−0.86	−13.950	26.457	30.449	1.532		0	1.60	0	0	
587731185135648996				2.30	0.65	−0.59	−13.810	24.775	28.568	1.456		0	1.74	0	0	
588015508201144501				2.79	0.90	−0.80	−13.690	26.153	29.830	1.412		0	1.78	0	0	
588015508201144513				1.77	0.71	−0.62	−13.580	26.673	30.307	1.395		0	1.60	0	0	
587731186209783863				0.90	0.48	−0.48	−13.300	26.871	31.118	1.630		0	0.63	2	1	Many strong NALs
588015509275803698	0.00	0.47	0.00	1.61	0.26	−0.16	−11.751	27.486	30.690	1.230	2508.80	1	3.84	0	0	
588015509275869378				1.32	0.84	−0.77	−13.410	27.688	31.542	1.480		0	1.12	0	1	

Notes. (1) SDSS Object ID, (2) SDSS R.A. (J2000), (3) SDSS decl. (J2000), (4) SDSS asinh mag_psf i, dereddened, (5) photometric redshift (see, Weinstein et al. 2004), (6) photometric redshift range probability, (7) lower limit of photometric redshift range, (8) upper limit of photometric redshift range, (9) best redshift: spectroscopic if different than $z_{\rm phot}$, (10) reference for spectroscopic redshift—S: SDSS, O: ChaMP, R: published reference from NED, (11) ChaMP IAU source name, (12) ChaMP internal source ID, format XSooooocBc_nnn where ooooo is *Chandra* obsid, c is ACIS CCD ID, and nnn is source ID on that CCD, (13) *Chandra* OAA in arcmin, (14) net 0.3–8 keV source counts, (15) rms uncertainty on net counts, (16) vignetting-corrected exposure time in ks, (17) galactic column in units 10^{20} cm^{-2}, (18) best-fit X-ray intrinsic column in 10^{22} cm^{-2}, only included four counts > 200, (19) 90% upper limit on intrinsic column in 10^{22} cm^{-2}, (20) 90% lower limit on intrinsic column in 10^{22} cm^{-2}, (21) best-fit X-ray power-law index Γ, (22) 90% upper limit on Γ, (23) 90% lower limit on Γ, (24) log X-ray flux (0.5–8 keV) in erg cm^{-2} s^{-1}, (25) log X-ray luminosity at 2 keV in erg s^{-1} Hz^{-1}, (26) log optical/UV luminosity at 2500 Å in erg s^{-1} Hz^{-1}, (27) $\alpha_{\rm ox}$, the optical/UV to X-ray spectral index, (28) 20 cm radio flux in mJy from FIRST or NVSS, (29) radio extent flag, (30) radio loudness R, (31) spectral class: 1, BAL; 2, NAL; 3, NLS1, (32) 1, intended *Chandra* PI target, (33) comments.
(This table is available in its entirety in a machine-readable form in the online journal. A portion is shown here for guidance regarding its form and content.)
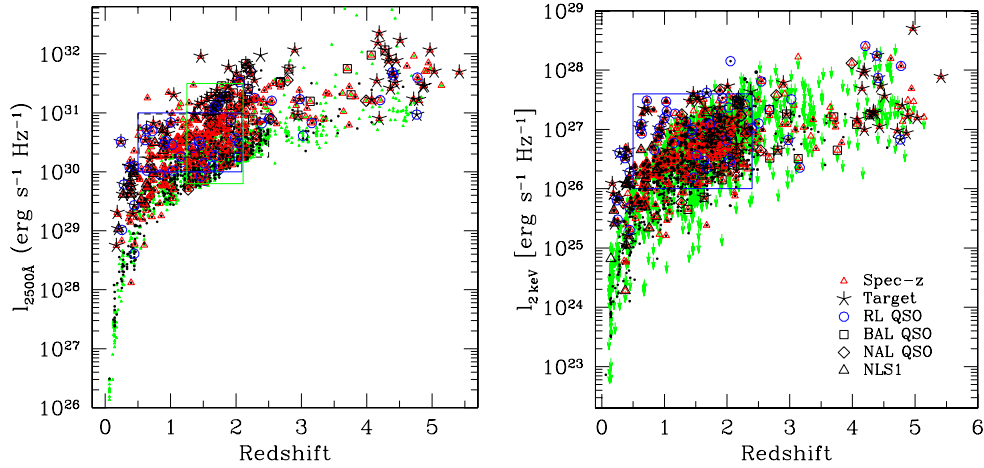
Figure 6. Luminosity at 2500 Å (left) and 2 keV (right) vs. redshift for the SDSS/ChaMP in the Main sample. Above $z \sim 2.5$, the number of QSOs declines steeply, due to the SDSS magnitude limit and due to the decreased efficiency of the photometric selection algorithm as it crosses the stellar color locus (see Figure 8 and Richards et al. 2002). These plots show 56 QSOs with $z > 3$, of which 34 are new serendipitous detections. X-ray upper limits are shown as small green triangles here. See Figure 3 for symbol types. The dashed black rectangle surrounds the zBoxDet sample, a portion of the $l_{2500\,\text{Å}} - z$ plane chosen to test for redshift dependence. The green rectangle "LoptBox" surrounds the LoBox sample, used to test for dependence on $l_{2500\,\text{Å}}$. The blue rectangle surrounds the zLxBox sample, chosen to avoid X-ray flux limit bias.

(A color version of this figure is available in the online journal.)
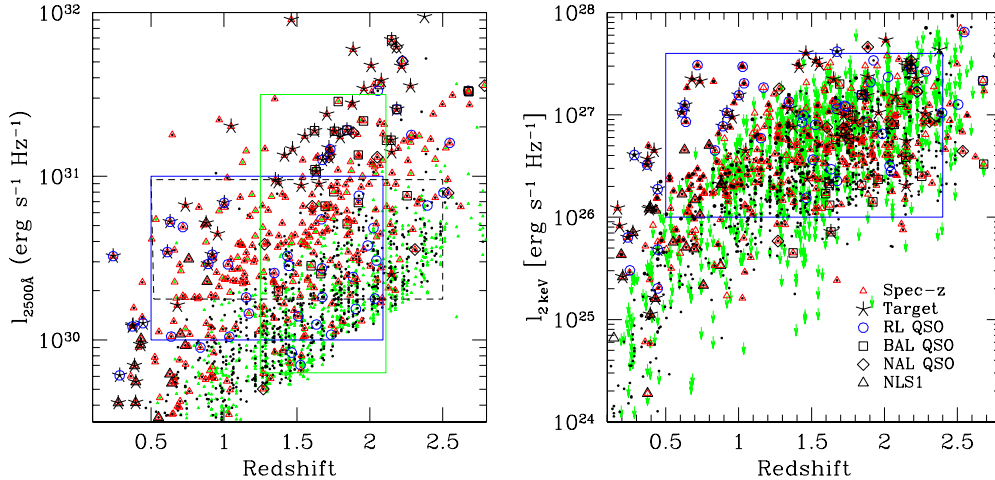
Figure 7. Left: zoom-in of 2500 Å luminosity vs. redshift. Objects with spectroscopic redshifts (open red triangles) tend to be at high optical luminosities by selection. Detectably radio-loud QSOs are shown with open blue circles. See Figure 3 for symbol types. BAL QSOs (open black squares) are mostly detected at $z > 1.6$ where the CIV region enters the optical bandpass. There appears to be no preference of BAL QSOs for high optical luminosity, apart from the bias caused by *Chandra* target selection. Right: zoom-in of 2 keV luminosity vs. redshift. Here, the RL QSOs clearly populate the upper luminosity envelope. BAL QSOs are preferentially X-ray quiet, unlike the QSOs with NALs only (open diamonds).

(A color version of this figure is available in the online journal.)

FIRST (5″), *FIRST* detection algorithms may exclude some of the extended source flux as background, so we include the NVSS fluxes for these 19 objects, and summed *FIRST* fluxes for those remaining.

Following Ivezić et al. (2002), we adopt a radio-loudness parameter R as the logarithm of the ratio of the radio to optical monochromatic flux: $R = \log(F_{20\,\text{cm}}/F_i) = 0.4(i - m_{20\,\text{cm}})$, where $m_{20\,\text{cm}}$ is the radio AB magnitude (Oke & Gunn 1983), $m_{20\,\text{cm}} = -2.5\log(F_{20\,\text{cm}}/3631\,\text{Jy})$ calculated from the integrated radio flux density, and i is the SDSS i-band magnitude, corrected for Galactic extinction. We adopt a radio-loudness threshold $R = 1.6$. Thus there are 72 QSOs in the Main sample with radio detections, of which 57 (79%) are radio loud. For the MainDet sample (detections only), there are 55 radio-detected QSOs, of which 43 (78%) are radio-loud. Figure 10 shows radio loudness versus redshift for the MainDet sample. Many of the radio upper limits are near our adopted radio loudness threshold.

Given the ($\sim$ 1 mJy) source detection limit of the *FIRST* Survey, all RL QSOs will be detected to about $i \sim 20.4$ mag. For the magnitude range $17 < i < 20$ where the statistics are good and the *FIRST* is sensitive to all RL QSOs, we find 41 of 529 ($8 \pm 1\%$) such QSOs from the MainDet sample are detected by the *FIRST*, with 29 (5.4%) that are radio loud. Since the 34% of our full the MainDet sample that is fainter than $i = 20.4$ suffers from incomplete radio-loudness measurements, some 2% may be unidentified RL QSOs. A similar fraction pertains if we count X-ray nondetections as well (the Main sample).

3.3. Broad and Narrow Absorption Line Quasars

We identified QSOs with BALs and NALs directly by visual inspection of QSOs with spectroscopy, finding 16 BAL and 11 NAL QSOs in the MainDet sample. Ten (two) of the BAL (NAL) QSOs were the *Chandra* PI targets.
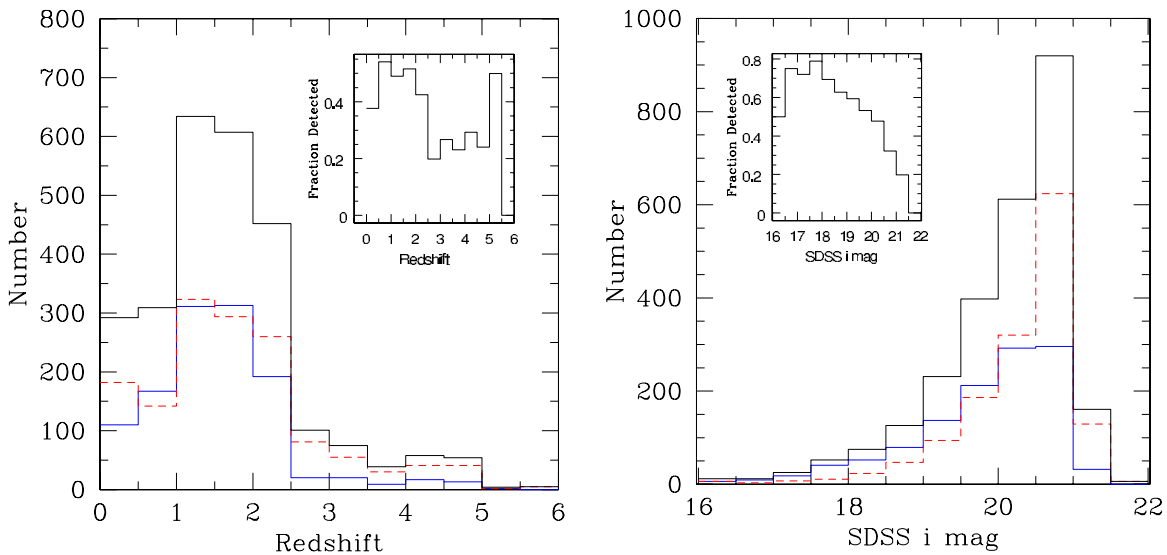
Figure 8. Left: histogram of redshifts for detected (solid blue), nondetected (red dashed), and all (black solid) QSOs in the MainDet sample. We tally the "best" redshift for each object (i.e., spectroscopic redshifts are always used when available). Above $z \sim 2.5$, the number of QSOs declines steeply, due to the decreased efficiency of the photometric selection algorithm as it crosses the stellar color locus (Richards et al. 2002). The inset shows the detected fraction as a function of redshift. Right: histogram of SDSS i mag for detected (solid blue), nondetected (red dashed), and all (black solid) QSOs. The inset shows the detected fraction as a function of magnitude.

(A color version of this figure is available in the online journal.)
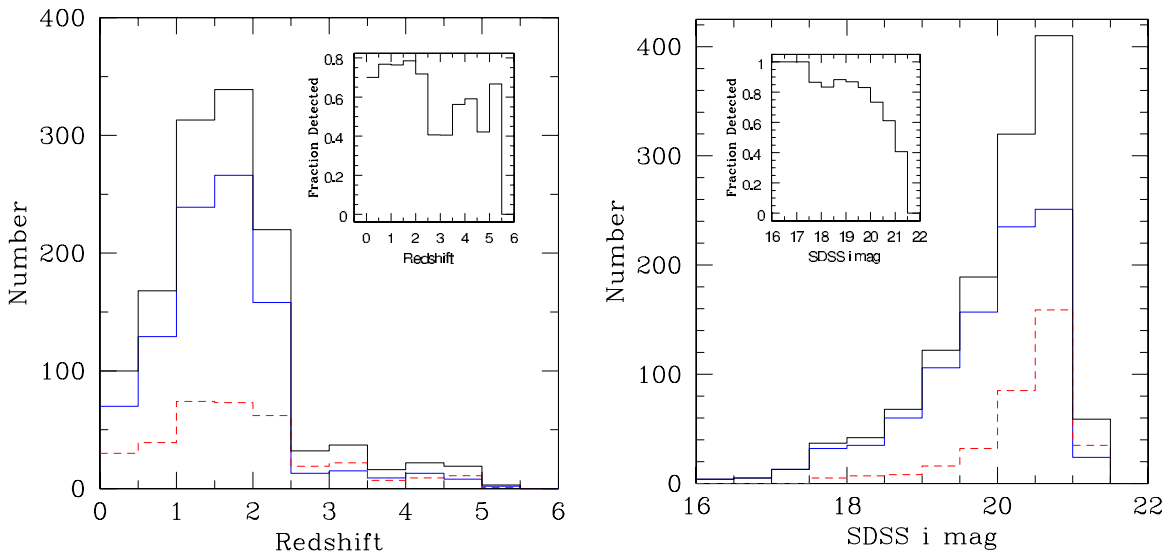
Figure 9. Left: histogram of redshifts for detected (solid blue), nondetected (red dashed), and all (black solid) QSOs, after restriction to obsids with $T > 4$ ks and QSOs with OAA less than 12′ (the D2L sample). The inset shows the detected fraction as a function of redshift. Right: histogram of SDSS i mag for detected (solid blue), nondetected (red dashed), and all (black solid) QSOs. The inset shows the detected fraction as a function of magnitude.

(A color version of this figure is available in the online journal.)

The best estimates to date of the raw BAL QSO fraction among optically selected quasars range from about 13–20% (Reichard et al. 2003; Hewett & Foltz 2003). From the SDSS DR3 sample of Trump et al. (2006), Knigge et al. (2008) carefully define what is a BAL QSO and correct for a variety of selection effects to derive an estimate of the *intrinsic* BAL QSO fraction of 17% ± 3. The vast majority of BAL QSOs in the SDSS are above redshift 1.6 because only then does the CIV absorption enter the spectroscopic bandpass.[19] If we determine our BAL QSO fraction in the MainDet sample by only counting the serendipitous (nontarget) QSOs with

$z > 1.6$ and spectroscopic redshifts, we find just 4 out of 119 QSOs with BALs. Even with sensitive X-ray observations such as these, X-ray selection is strongly biased against the highly ionized absorbing columns along the line of sight toward the X-ray emitting regions of BAL QSOs. Of the 24 absorbed (BAL or NAL) QSOs, two are detectably radio loud; SDSS J171419.24+611944.5—a BAL QSO—and SDSS J171535.96+632336.0—a NAL QSO—are targets selected (by *Chandra* PI Richards) as reddened QSOs.

3.4. Narrow-Line Seyfert 1s

X-rays from NLS1s are of particular interest because they were thought to show marked variability and strong soft

---

[19] A much smaller number of the rare low-ionization BAL QSOs (with BALs just blueward of Mg II) are found at lower redshifts.
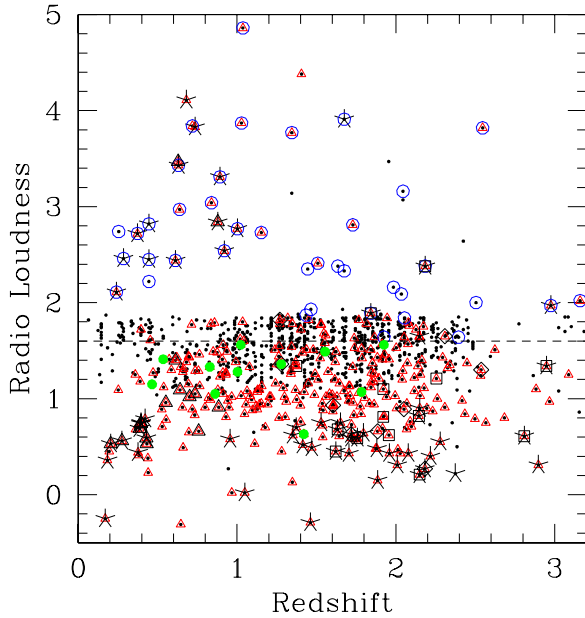
Figure 10. Radio-loudness vs. redshift for the MainDet sample (detections). Radio-loud objects $R > 1.6$ are shown with open blue circles. Radio-quiet but *FIRST* radio-detected objects are shown as filled green circles. All other symbols (described in Figure 3) have radio flux upper limits only. Note that most *Chandra* targets are distinctly either loud or quiet, highlighting a bias in the target subsamples.

(A color version of this figure is available in the online journal.)

X-ray excesses (e.g., Green et al. 1993; Boller et al. 1996). NLS1s are proposed to be at one extreme of the so-called (Boroson & Green 1992) "eigenvector 1," which has been suggested to correspond to low SMBH masses (Grupe et al. 2004) and/or high (near-Eddington) accretion rates (Boroson 2002).

For objects with SDSS spectra encompassing Hβ ($z < 0.9$), we identify as NLS1s (Osterbrock & Pogge 1985) those objects with FWHM(Hβ) < 2000 km s^{-1} and line flux ratio [O III]/H$\beta <$ 3. The FWHM measurements are obtained via FWHM = $2.35\,c\,\sigma/\lambda_0/(1 + z)$, where σ^2 is the variance of the Gaussian curve that fits the Hβ emission line, z is the redshift, and λ_0 is the rest-frame wavelength of the Hβ line (4863 Å). We extract measurements of σ (in Å) and line fluxes from the SDSS DR6 SpecLine table.

Our MainDet sample contains at least 19 NLS1s (those with spectroscopy in the redshift range to include Hβ). Among the nondetections, we identify three more. Six of these 22 objects are targets described in Williams et al. (2004), and SDSS J125140.33+000210.8 was a target selected (by *Chandra* PI Richards) as a dust-reddened QSO. The Williams et al. (2004) sample consisted of 17 SDSS NLS1s selected from the *ROSAT* All Sky Survey to be X-ray weak. Their study confirmed earlier suggestions that strong, ultrasoft X-ray emission is not a universal characteristic of NLS1s.

We therefore present here new results for a sample of 15 SDSS NLS1s observed by *Chandra*. This admittedly small sample is nevertheless the largest published sample of optically selected NLS1s with unbiased X-ray observations. The sample of Williams et al. (2004) was selected to be X-ray weak, while the Grupe et al. (2004) ROSAT sample was selected to have strong soft X-ray emission. We find no evidence for unusual SEDs from the distributions of either $\alpha_{\rm ox}$ or Γ.

4. OPTICAL COLORS AND REDDENING

In Figure 11, we plot the $(g - i)$ colors of the matched SDSS/ChaMP QSO sample as a function of redshift, and compare to the optical-only sample.[20] The *Chandra*-detected sample does not show significantly different colors from the full optical sample. This likely attests to (1) the sensitivity of the *Chandra* imaging relative to the magnitude limit of the optical sample and (2) the fact that Type 1 QSOs are largely unabsorbed in both the optical and X-ray regimes.

The right panel of Figure 11 shows that 10 of 14 BAL QSOs are above the $\Delta(g - i) = 0$ line. This reflects that SDSS BAL QSOs tend to be redder than average (Reichard et al. 2003; Dai et al. 2007). Most of the RL QSOs are also redder than average. Richards et al. (2001) found a higher fraction of intrinsically reddened quasars among those with *FIRST* detections. Ivezić et al. (2002) found that RL QSOs are redder than the mean (at any given redshift) in $(g - i)$ by 0.09 ± 0.02 mag. Figure 11 confirms a similar trend in the X-ray detected SDSS/ChaMP sample. At the same time, a small number of RL QSOs are found on the blue extreme of the color-excess distribution. These trends are fully consistent with the detailed results found by stacking *FIRST* images of SDSS quasars (White et al. 2007), independent of X-ray properties.

5. X-RAY SPECTRAL FITTING WITH yaxx

Besides comparing the broadband multiwavelength properties of QSOs, *Chandra* imaging provides X-ray spectral resolution capable of yielding significant constraints on the properties of emission arising nearest the SMBH. While the ChaMP calculates hardness ratios (HRs) and appropriate errors for every source, these can be difficult to interpret, since HR convolves the intrinsic quasar SED with telescope and instrument response and does not take redshift or Galactic column $N_H^{\rm Gal}$ into account. A direct spectral fit of the counts distribution using the full instrument calibration, known redshift, and $N_H^{\rm Gal}$ provides a much more direct measurement of quasar properties. Note that even in the low-count regime, one can obtain robust estimates of fit parameter uncertainties using the Cash (1979) fit statistic.

We use an automated procedure to extract the spectrum and fit up to three models to the data. For all objects in the Matched sample, we first define a circular source region centered on the X-ray source which contains 95% of 1.5 keV photons at the given OAA. An annular background region is also centered on the source with a width of 20″. We exclude any nearby sources from both the source and background regions. We then use CIAO[21] tool psextract to create a PHA (pulse height amplitude) spectrum covering the energy range 0.4–8 keV.

Spectral fitting is done using the CIAO *Sherpa*[22] tool in an automated script known as yaxx[23] (Aldcroft 2006). All of the spectral models contain an appropriate Galactic neutral absorber. For all sources we first fit two power-law models which include a Galactic absorption component frozen at the 21 cm value[24]: (1) fitting photon index Γ, with no intrinsic absorption

---

[20] The optical-only sample refers to all SDSS QSOs within ∼20′ of all *Chandra* pointings, regardless of whether its position falls on an ACIS CCD. We use a 9th-order polynomial fit to the optical-only sample with the following coefficients: 0.698892, 3.011733, −20.358267, 37.850353, −33.617121, 16.652032, −4.861889, 0.833027, −0.077526, and 0.003026.
[21] http://cxc.harvard.edu/ciao
[22] http://cxc.harvard.edu/sherpa
[23] http://cxc.harvard.edu/contrib/yaxx
[24] Neutral Galactic column density $N_H^{\rm Gal}$ taken from Dickey & Lockman (1990) for the *Chandra* aim-point position on the sky.

Table 3
Properties of SDSS Quasars with *Chandra* Limits

SDSS Obj ID (1)	R.A. (J2000) (2)	Decl. (3)	i (4)	z_{phot} (5)	P_z (6)	z_{lo} (7)	z_{hi} (8)	z_{best} (9)	Spec Ref (10)	obsid (11)	ccdid (12)	OAA (13)	counts < (14)	Exposure (15)	N_H^{Gal} (16)	log f_x < (17)	log l_{2keV} < (18)	log $l_{2500 Å}$ (19)	α_{ox} > (20)	f_{20cm} (21)	R (22)	Class (23)	Notes (24)
588015510343385295	0.56337	0.909429	20.956	4.6050	0.949	4.440	5.22	4.6050		4861	7	6.4	16.0	4.5	2.5	−13.650	27.554	30.856	1.268		1.82	0	
588015510343385302	0.63485	0.870704	20.819	2.2250	0.415	1.840	2.70	2.2250		4861	7	2.8	10.0	4.6	2.5	−13.865	26.581	30.311	1.432		1.77	0	
588015509270823376	3.32406	0.057045	20.984	0.0650	0.616	0.060	0.12	0.0650		4829	7	3.5	11.1	6.0	5.6	−13.926	22.955	26.290	1.280		1.83	0	
588015509270888717	3.40998	0.141416	20.457	1.4450	0.615	0.960	1.61	1.4450		4829	3	9.0	20.2	4.4	5.6	−13.239	26.747	30.023	1.258		1.62	0	
588015509270888725	3.45158	0.098009	20.804	1.4950	0.774	0.950	2.22	1.4950		4829	3	10.8	22.7	4.6	5.6	−13.211	26.811	29.915	1.191		1.76	0	
587730775501504550	5.00208	15.852781	19.190	1.6850	0.915	1.440	2.11	1.7510	S	1595	5	10.7	25.3	5.3	4.2	−13.405	26.786	30.742	1.519		1.12	0	
587727180601295054	10.04659	−9.111831	20.220	2.0950	0.653	1.290	2.26	2.0950		4888	3	7.5	17.2	7.8	3.4	−13.668	26.714	30.495	1.452		1.53	0	
587727180601557048	10.60443	−8.983756	19.739	1.8750	0.916	1.590	2.13	1.8750		4886	2	9.9	22.6	6.9	3.6	−13.498	26.766	30.586	1.466		1.34	0	
587727227305394556	10.73418	−9.141124	20.920	0.1450	0.370	0.140	0.25	0.1450		4886	1	2.3	9.4	7.9	3.6	−13.930	23.694	27.029	1.280		1.81	0	
587727180601622916	10.82587	−9.032790	20.550	2.8550	0.866	2.520	3.26	2.8550		4886	0	8.1	17.7	7.0	3.6	−13.605	27.104	30.574	1.332		1.66	0	
587731185135649019	12.55619	−0.978559	20.734	0.3950	0.575	0.240	0.98	0.3950		4825	7	6.2	15.1	11.4	2.1	−14.075	24.536	28.869	1.663		1.73	0	
588015508201144424	12.68671	−0.838214	20.077	0.5850	0.525	0.420	0.68	0.5850		4825	3	10.0	22.7	5.9	2.1	−13.317	25.702	29.374	1.410		1.47	0	
588015509275279576	13.48778	0.041851	21.014	2.3550	0.485	2.080	2.73	2.3550		4830	6	5.1	12.8	5.0	1.9	−13.635	26.871	30.327	1.327		1.85	0	
587731186209849918	13.50874	−0.132789	20.138	4.6750	0.958	4.480	4.87	4.6750		4830	7	5.7	14.0	6.2	1.9	−13.843	27.376	31.176	1.459		1.49	0	
587731151532454189	19.71203	−0.963115	20.433	2.3950	0.849	2.190	2.92	2.3950		4963	7	4.1	15.0	36.9	14.1	−14.575	25.949	30.534	1.760		1.61	0	
587731511532454208	19.75317	−0.964191	20.711	0.1250	0.503	0.120	0.25	0.1250		4963	7	4.2	14.8	36.5	14.1	−14.577	22.908	27.428	1.735		1.72	0	
588015507667419343	19.83900	−1.181540	19.716	1.4350	0.927	1.140	1.53	1.4350		4963	5	11.1	43.3	20.3	14.1	−13.737	26.241	30.318	1.565		1.33	0	
587727884161581293	29.96522	−8.803312	20.815	0.1250	0.597	0.120	0.26	0.1250		6106	3	3.2	12.0	32.7	15.9	−14.453	23.032	27.465	1.702		1.77	0	
587727883893211318	30.05424	−8.839227	20.380	1.8250	0.479	1.440	2.01	1.8250		6106	2	5.0	13.9	29.1	15.9	−14.342	25.893	30.304	1.693		1.59	0	
587727178999398623	30.28336	−9.408542	20.874	2.4850	0.686	2.060	2.76	2.4850		3772	7	3.5	11.4	13.2	24.2	−14.278	26.284	30.470	1.607		1.79	0	
587731512611897674	32.80721	−0.133716	20.592	1.4450	0.561	0.960	1.66	1.4450		2081	7	3.2	10.2	4.0	2.7	−13.872	26.113	29.957	1.475		1.68	0	
587731513691013244	45.00239	0.807781	16.531	4.3850	0.990	4.190	4.51	4.3850		4145	7	0.6	7.7	4.0	7.0	−13.875	27.278	32.749	2.100		0.05	0	
587731512083349864	51.75811	−0.573625	20.969	1.1150	0.702	0.620	1.66	1.1150		5810	2	8.4	18.3	7.8	6.7	−13.624	26.083	29.515	1.317		1.83	0	
587728906098377011	115.26597	31.160109	18.733	3.8450	0.971	3.370	4.35	3.8450		0377	7	3.4	11.7	26.1	4.2	−14.530	26.488	31.669	1.989		0.93	0	
587728906098376844	115.31801	31.184168	20.380	4.8350	0.983	4.510	5.52	4.8350		0377	7	1.8	9.8	25.5	4.2	−14.595	26.658	31.268	1.770		1.51	0	
588007005767532860	116.33380	39.501996	20.363	0.8250	0.582	0.390	1.01	0.8250		6111	1	5.6	14.5	28.7	8.3	−14.298	25.086	29.585	1.727		1.59	0	
588007005767532880	116.44541	39.466243	20.179	2.0250	0.738	1.820	2.19	2.0250		6111	1	10.7	34.7	35.6	8.3	−14.014	26.333	30.480	1.592		1.51	0	
587731680110052241	116.73920	27.665360	20.778	4.6050	0.984	4.440	5.19	4.6050		3561	7	3.2	10.4	4.4	4.7	−13.833	27.371	31.001	1.394		1.75	0	
587725470127095818	118.81215	41.058484	19.824	1.6150	0.725	1.440	1.95	1.6150		3032	2	11.5	25.7	4.1	8.5	−13.144	26.960	30.331	1.294		1.37	0	

Notes. (1) SDSS object ID, (2) SDSS R.A. (J2000), (3) SDSS decl. (J2000), (4) SDSS asinh mag_psf i, dereddened, (5) photometric redshift (see Weinstein et al. 2004), (6) photometric redshift range probability, (7) lower limit of photometric redshift range, (8) upper limit of photometric redshift range, (9) best redshift: spectroscopic if different than z_{phot}, (10) reference for spectroscopic redshift—S: SDSS, O: ChaMP, R: published reference from NED, (11) *Chandra* observation ID (obsid), (12) ACIS CCD id, (13) *Chandra* OAA in arcmin, (14) 99% counts upper limit the 0.3–8 keV range, (15) vignetting-corrected exposure time in ks, (16) galactic column in units 10^{20}cm^{-2}, (17) log upper limit to the X-ray flux (0.5–8 keV) in erg cm^{-2} s^{-1}, (18) log upper limit to the X-ray luminosity at 2 keV in erg s^{-1} Hz^{-1}, (19) log optical/UV luminosity at 2500 Å in erg s^{-1} Hz^{-1}, (20) α_{ox}, the optical/UV to X-ray spectral index, (21) 20 cm radio flux in mJy from *FIRST*, (22) radio loudness, (23) class: 1, BAL; 2, NAL; 3, NLS1, (24) comments.

(This table is available in its entirety in a machine-readable form in the online journal. A portion is shown here for guidance regarding its form and content.)
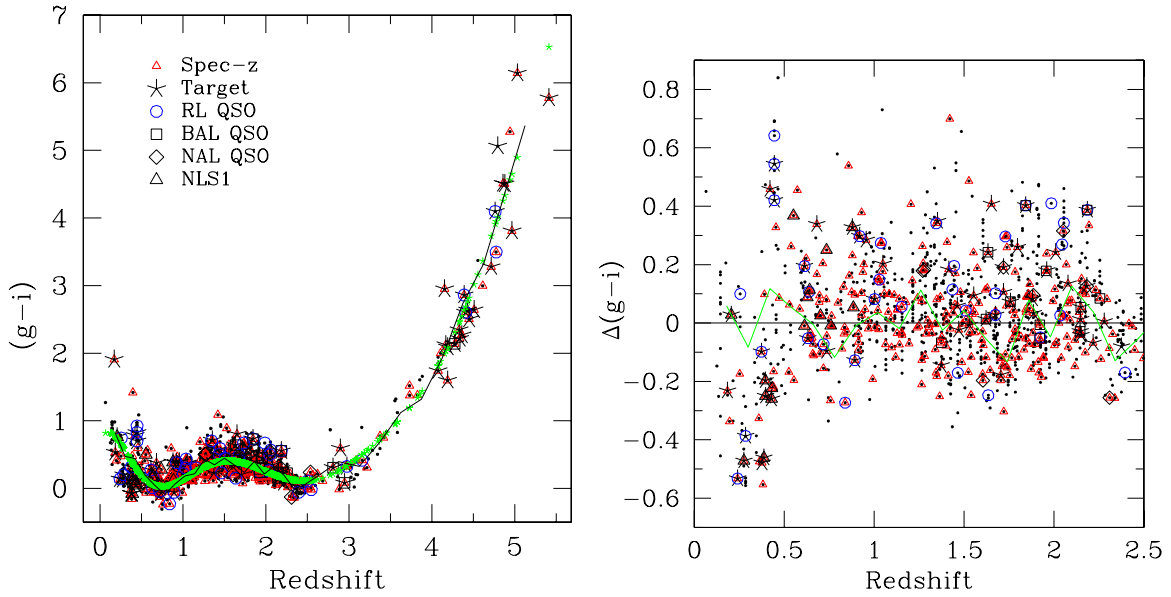
Figure 11. Left: SDSS $(g - i)$ color vs. best redshift. Symbols show individual QSOs in the SDSS/ChaMP the MainDet sample. The black line shows the mean color at each redshift (in redshift bins of 0.12 for $z < 2.5$ and 0.25 for higher redshifts) for the full optical QSO sample (regardless of *Chandra* imaging). We derive a smooth (9th-order) polynomial fit to those means, whose value is plotted as the "expected" $(g - i)$ with a green asterisk (at the redshift of each actual QSO). Right: the color excess $\Delta(g - i)$ (the difference between the actual and "expected" $(g - i)$ color) is plotted against redshift for a limited redshift range, to show highlights. The residuals of the polynomial fit to the mean binned $(g - i)$ of the full optical sample are shown connected by a solid green line. See Figure 3 for symbol types. Most targets, BAL QSOs, and RL QSOs are redder than average.

(A color version of this figure is available in the online journal.)

component (model "PL") and (2) fitting an intrinsic absorber with neutral column N_H^{intr} at the source redshift, with photon index frozen at $\Gamma = 1.9$ (model "PLfix"). Allowed fit ranges are $-1.5 < \Gamma < 3.5$ for PL and $10^{18} < N_H^{intr} < 10^{25}$ for PLfix. These fits use the Powell optimization method, and provide a robust and reliable one-parameter characterization of the spectral shape for any number of counts. Spectra with less than 100 net counts[25] were fit using the ungrouped data with Cash statistics (Cash 1979). Spectra with more than 100 counts were grouped to a minimum of 16 counts per bin and fit using the χ^2 statistic with variance computed from the data.

Finally, X-ray spectra with over 200 counts were also fit with a two-parameter absorbed power law where both Γ and the N_H^{Gal} were free to vary within the above ranges (model "PL_abs").

5.1. X-Ray Spectral Continuum Measurements

We compile "best-PL" measurements, where for fewer than 200 counts, we use Γ from the PL (N_H^{intr} fixed at zero) fits and for higher count sources we use PL_abs (both Γ and N_H^{intr} free). In the MainDet sample there are 156 sources with 200 counts or more. High-count objects are found scattered at all luminosities below $z \sim 2.5$. QSOs with more than 200 counts (0.5–8 keV) with both Γ and N_H^{intr} fits in yaxx, are well-distributed in $l_{2\,keV}$ amongst the detections due to the wide range of exposure times.

The mean Γ for all the 1135 QSOs in the MainDet sample is 1.94 ± 0.02 with median 1.93. Means and medians for the MainDet sample and the subsamples discussed in this section are listed in Table 4. The typical (median) error in Γ, $\Delta\Gamma \sim 0.5$, is similar to the dispersion 0.54 in best-fit values of Γ. If we limit the sample to the 314 sources with more than 100 counts,

the typical error is 0.32, with no change in mean or median Γ. The Γ distribution that we find is similar to that found recently for smaller samples of broad-line AGNs (BLAGNs). Just et al. (2007) studied a sample of luminous optically selected quasars observed by *Chandra*, *ROSAT*, and *XMM-Newton*, and found $\langle\Gamma\rangle = 1.92 \pm 0.09$ for 42 QSOs. Mainieri et al. (2007) studied a sample of 58 *X-ray-selected* BLAGNs in the *XMM-COSMOS* fields, and found $\langle\Gamma\rangle = 2.09$ with a dispersion of ~0.26. Page (2006) found $\langle\Gamma\rangle = 2.0 \pm 0.1$ with a dispersion of ~0.36 for 50 X-ray-selected BLAGN in the 13^H *XMM-Newton/Chandra* deep field.

Figure 12 shows a histogram of best-fit power-law slopes for several interesting subsamples of QSOs from both the MainDet sample and from the noTDet sample which omits PI targets. The mean and median values for these subsamples are listed in Table 4. We do not separately plot the radio-quiet (RQ) QSO sample, since it follows quite closely the shape of the full sample histogram.

For 43 detected RL QSOs in the MainDet sample, the nominal mean slope is $\langle\Gamma\rangle = 1.73 \pm 0.05$ with median 1.65, with a distribution significantly flatter than for the 704 definitively RQ QSOs ($\langle\Gamma\rangle = 1.91 \pm 0.02$) in the MainDet sample, using the two-sample tests described in Section 6.1.1. RL QSOs are known to have flatter high energy continua from previous work (e.g., Reeves & Turner 2000).

For the 15 known BAL QSOs in the MainDet sample, the nominal mean slope is $\langle\Gamma\rangle = 1.35 \pm 0.15$ with median 1.3, and the distribution is significantly different than for the full MainDet sample (minus BALs, NALs, and NLS1), using the two-sample tests described in Section 6.1.1. The difference is even more significant ($P_{max} < 0.01\%$) when comparing only to the 667 definitively RQ QSOs ($RL < 1.6$). Since the mean (median) number of (0.5–8 keV) counts for BAL QSOs is just 27 (15), the nominally lower Γ likely reflects undetected absorption (Green et al. 2001; Gallagher et al. 2002).

---

[25] Source counts derived from yaxx may differ at the $\sim1\%$ level from those derived by ChaMP XPIPE photometry, due to slightly different background region conventions.
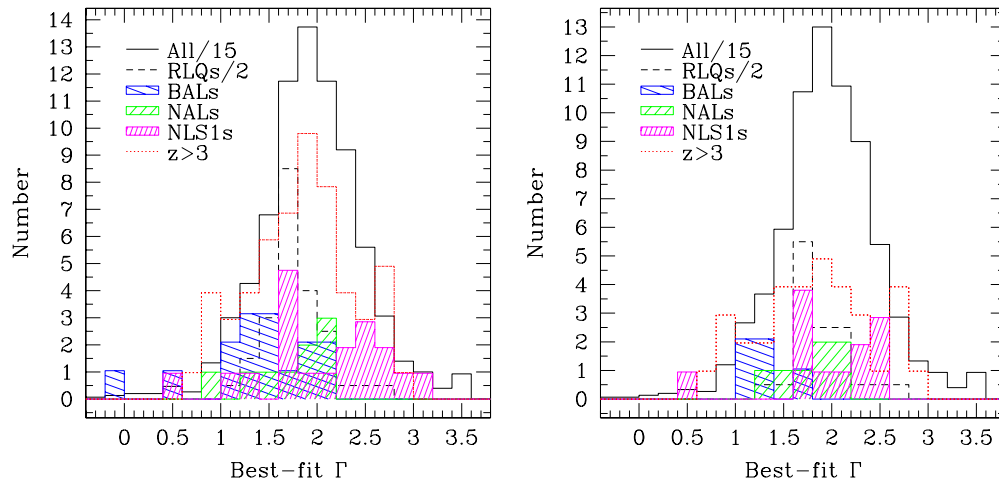
Figure 12. Left: histogram of best-fit X-ray spectral power-law slope Γ (best-PL) for the MainDet sample. The full sample (black solid) histogram has been divided by 15, and the RL QSO (long-dashed black) histogram by 2, for ease of comparison with smaller subsamples. BAL QSOs (blue down-slash shading) show very flat slopes, due to strong intrinsic absorption. The NAL distribution (green up-slash shading) suggests a possible bimodality. Neither the NAL nor the NLS1 (magenta dense shading) nor the high redshift (short-dashed red) histograms are significantly different, by the Kolmogorov–Smirnov (K-S) test from the full sample distribution. Right: the same plot, but for the noTDet sample which omits PI targets. The RL QSO distribution is less distinct here, and the softest (largest Γ) NLS1s disappear.

(A color version of this figure is available in the online journal.)

Table 4
Quasar Sample Univariate Results

Sample[a]	N	Mean	Error[b]	Median	P_{max}[c](%)
		Γ Distributions[d]			
MainDet	1135	1.94	0.02	1.93	. . .
RQ	704	1.91	0.02	1.86	0.2
RL	43	1.73	0.05	1.65	0.2
BAL	15	1.35	0.15	1.30	0.05
NAL	9	1.68	0.13	1.75	19
NLS1	19	2.01	0.15	1.95	35
$z > 3$	56	1.80	0.07	1.76	21
		α_{ox} Distributions			
D2L	1269	1.421	0.005	1.365	. . .
RQ	680	1.527	0.008	1.452	0.0
RL	31	1.382	0.030	1.392	0.0
BAL	23	1.717	0.028	1.664	0.0
NAL	8	1.463	0.056	1.500	49
NLS1	19	1.540	0.080	1.433	24
$z > 3$	47	1.817	0.077	1.786	55

Notes.

[a] For each parameter tested, the numeric sample at the top is the parent for comparison subsamples below. The RL subsamples are tested against non-RL QSOs from the parent sample. The remaining three QSO subsamples for each parameter are tested against the parent sample excluding all four QSO subtypes.
[b] Error in the mean from the Kaplan–Meier estimator as implemented in ASURV. An estimate of the dispersion can be obtained by multiplying this by $\sqrt{N-1}$.
[c] The maximum probability for the null hypothesis (of indistinguishable samples) from three tests described in Section 6.1.1. Only for $P_{max} < 5$ do we consider the distributions significantly different. RL and RQ samples are contrasted to each other. Other samples are compared to their parent sample (MainDet or D2L) $-X$, where X = BALs + NALs + NLS1s, except for BALs, whose parent sample is RQ QSOs only.
[d] These are distributions of "best-PL" measurements, best-fit Γ, which always includes N_H^{Gal}, and also includes N_H^{intr} for 0.5–8 keV counts > 200.

The mean slope $\langle\Gamma\rangle = 1.68 \pm 0.13$ with median 1.75 for the nine known NALs in the MainDet sample is indistinguishable from the full MainDet sample (minus BALs, NALs, and NLS1), but the NAL statistics are poor. On the other hand, a smaller, non-overlapping sample of NALs observed by *Chandra* published by Misawa et al. (2008) agrees that the X-ray properties of intrinsic NAL quasars are indistinguishable from those of the larger quasar population.

For the 19 known NLS1s in the MainDet sample, the nominal mean slope is $\langle\Gamma\rangle = 2.01 \pm 0.15$ with median 1.95, indistinguishable from the comparison sample (MainDet sample minus BALs, NALs, and NLS1).

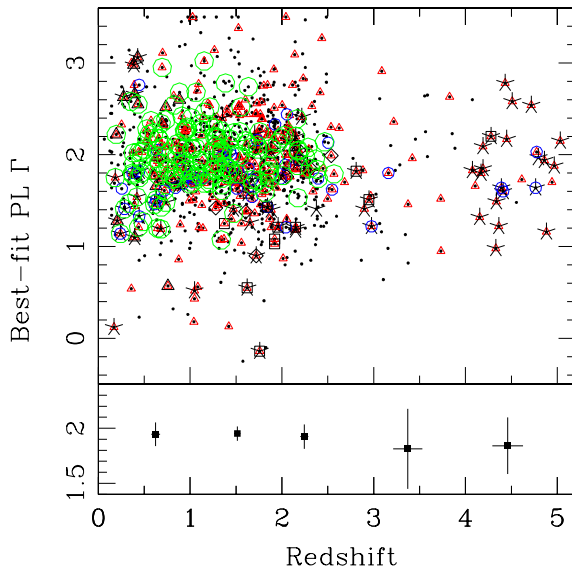### 5.1.1. X-Ray Spectral Evolution

No signs of evolution have been detected for the intrinsic power-law slope Γ of QSOs: $z > 4$ samples (Vignali et al. 2005; Shemmer et al. 2006) show $\Gamma \sim 2$, just like those at lower redshifts (Reeves & Turner 2000). In a recent small sample of high (optical) luminosity QSOs (Just et al. 2007) also found no trend of Γ with redshift. A larger compilation also shows at best marginal signs of evolution, and only for well-chosen redshift ranges (Saez 2008).

Figure 13 shows Γ versus redshift both for the individual QSOs (top), and for subsamples (bottom) in fixed bins of Δz. We also try another binning, where we grow redshift bins from $z = 0$ until each bin has between 100 and 150 objects (except for the high-redshift bin $z > 3$ which has just 58). The largest difference between any of the bins is 0.17, whereas the typical rms dispersion in all bins is $\sim$0.5.
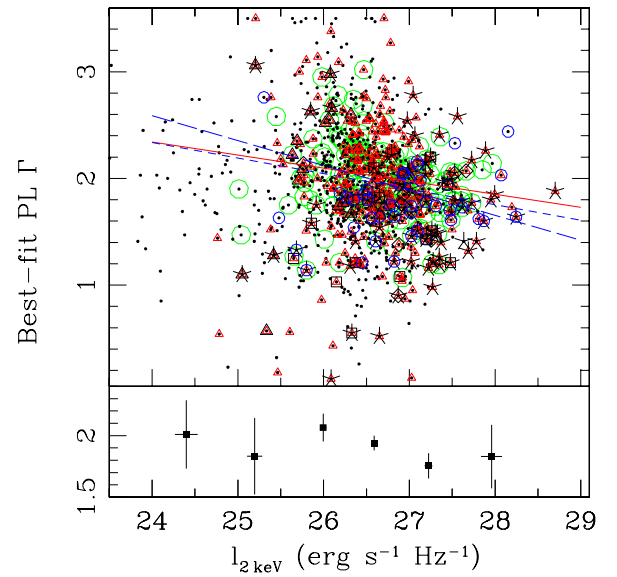
The noTDet sample and the NoRBDet sample remove contributions from targets, and from RL or absorbed QSOs, respectively. The HiCt sample is the subset of the MainDet sample with counts greater than 200, where fits for N_H^{intr} are also performed. This decreases the effect of QSOs that may appear to have hard Γ but are actually absorbed. The HiCtNoTRB sample also has only counts greater than 200, but further removes targets, RL, BAL, and NAL QSOs. We find no evidence for evolution; the null hypothesis (no correlation) cannot be rejected with $P < 8\%$ for any of samples 0, 1, 2, 20, or 21, which test possible contamination or biases from targets, RL, and/or absorbed QSOs.

Given that the typical uncertainty in Γ for a single QSO (~ 0.5) is comparable to the sample dispersion, simultaneous spectral fitting of subsamples of detected QSOs in bins of redshift (in the manner of Green et al. 2001) might improve

Figure 13. Top: best-fit X-ray spectral power-law slope Γ vs. redshift for the MainDet sample. The large open green circles show QSOs with more than 200 (0.5–8 keV) counts and simultaneous Γ–$N_H^{\rm intr}$ fits. No evidence is seen for evolution in Γ. See Figure 3 for symbol types. Dots to distinguish detections from limits in other plots are omitted here, since by definition all objects are detected. Radio-loud QSOs (open blue circles) tend to have flatter slopes. Some of the flattest slopes seen are for BAL QSOs (open black squares), due to their strong intrinsic absorption. Typical mean errors on Γ are $\sim$0.5 below $z = 2$, rising to 0.8 at the highest redshifts. Bottom: mean Γ values are shown at the mean redshift for QSOs in five redshift bins of width $\Delta z = 1$ for the MainDet sample. Error bars show the error in the means for both axes.

(A color version of this figure is available in the online journal.)

Table 5
Quasar Sample Bivariate Regression Results: $\Gamma(l_{2\,{\rm keV}})$ OLS

Sample	Slope	Error	Intercept	Error
MainDet	−0.1465	0.0199	5.8575	0.5276
noTDet	−0.1424	0.0188	5.7579	0.4959
HiCtNoTRBt	−0.1213	0.0497	5.2473	1.3333
NoRBDet	−0.1528	0.0262	6.0343	0.6980
hiLoLx	−0.2336	0.0388	8.1937	1.0337
HiCt	−0.1454	0.0472	5.8540	1.2679

Notes. Samples tested are arranged in the same order as in Table 1. OLS refers to the ordinary least-squares regression.

constraints, but such a project is both beyond the scope of this paper and probably unwarranted given the scarce evidence for evolution to date.

5.1.2. X-Ray Spectral Trend with X-Ray Luminosity

There is conflicting evidence as to whether Γ correlates with X-ray luminosity L_X (Dai et al. 2004; Page et al. 2004), or perhaps with Eddington ratio (Porquet et al. 2004; Kelly 2007b; Shemmer et al. 2008; Kelly et al. 2008). Saez (2008) find significant softening (increase) of Γ with luminosity in selected redshift ranges, for a combination of Type 1 and Type 2 X-ray-selected AGNs from the CDFs. Type 2 objects dominate numerically, especially at low L_X, and show larger scatter in Γ at all luminosities, so Type 2 objects dominate the trends that they observe. Our sample is complementary in that it treats only Type 1 QSOs, and provides the largest, most uniform such spectral study to date.

We detect a significant anticorrelation between Γ and $l_{2\,{\rm keV}}$ across a several subsamples (see Table 5 and Figure 14), but none

Figure 14. Top: best-fit X-ray spectral power-law slope Γ vs. X-ray luminosity for the MainDet sample. See Figure 3 for symbol types. The large open green circles show QSOs with more than 200 (0.5–8 keV) counts and simultaneous Γ–$N_H^{\rm intr}$ fits. A significant but shallow trend toward harder spectra (smaller Γ) is evident from the best-fit regression lines shown: the MainDet sample (red solid), the HiCtNoTRB sample with counts greater than 200 (blue short-dashed) or HiLoLx sample with log $l_{2500\text{Å}} > 29.8$ and $l_{2\,{\rm keV}} > 26$ (blue long-dashed). Fit parameters are shown in Table 5. Bottom: mean Γ values are shown at the mean luminosity for QSOs in six bins of width $\Delta l_X = 0.75$ for the MainDet sample. Error bars show the error in the means for both axes.

(A color version of this figure is available in the online journal.)

between Γ and either redshift or $l_{2500\,\text{Å}}$. The best-fit continuum slope Γ hardens (decreases) with increasing luminosity for the MainDet sample. Since Γ is itself used to calculate $l_{2\,{\rm keV}}$ via the standard X-ray power-law k-correction, there might be some danger that the apparent anticorrelation is induced. We investigate this in two ways. First we examine the range in the ratio of $l_{2\,{\rm keV}}$ calculated assuming our best-fit Γ k-correction to that calculated with a fixed $\Gamma = 1.9$. Across the full X-ray luminosity range, the different assumptions induce a change of $\sim$0.1 dex ($\sim$25%), insufficient to account for the observed trend. Second, we examine whether Γ correlates significantly with $l_{2500\,\text{Å}}$, which is clearly unaffected by the X-ray k-correction. There is indeed a significant trend in the MainDet sample (see Table 5).

One possibility is that the observed trend of Γ with luminosity might be due to an undetected increase in $N_H^{\rm intr}$. To test this, we examined the relationship in the HiCtNoTRB sample, the subset of the MainDet sample with counts greater than 200, where fits for $N_H^{\rm intr}$ are also performed. We do not claim that all absorption is detected in the HiCtNoTRB sample. However, if indeed undetected absorption caused the trend in the MainDet sample, we would expect the anticorrelation to weaken or flatten in the HiCtNoTRB sample. Instead, the anticorrelation is still significant, and the slope is actually steeper (see Table 5).

It is also conceivable that soft X-ray emission associated with star-formation activity might contaminate the sample at low luminosities. To test this, we create the HiLoLx sample with definitively QSO-like luminosities in both wavebands, i.e., log $l_{2500\,\text{Å}} > 29.8$ and $l_{2\,{\rm keV}} > 26$. For this sample, the anticorrelation remains strong and steep (see Table 5).

We speculate that the balance between thermal (accretion disk) and nonthermal X-ray emission may shift toward higher luminosities. If at high $l_{2\,{\rm keV}}$, nonthermal emission represents

a larger fraction of the emitted X-rays, we would expect a hardening (decrease) of Γ with luminosity, as is seen. We would also expect to find more RL QSOs at high $l_{2\,\mathrm{keV}}$, and we do. Since quasars such as RL QSOs with a larger fraction of nonthermal emission also show stronger X-ray emission relative to optical (smaller α_{ox}), we might expect a correlation between Γ and α_{ox} such that as the spectrum hardens, α_{ox} decreases. This is shown to be the case in Section 7.2. The idea of a significant nonthermal, probably jet-related, emission component even in RQ QSOs is not new. Blundell & Beasley (1998) found strong evidence from very long baseline array (VLBA) observations for jet-producing central engines in eight of the 12 RQ QSOs in their sample. Barvainis et al. (2005) find similarities between RL and RQ quasars spanning a host of radio indicators (variability, radio spectral index, and VLBI-scale components), suggesting that the physics of radio emission in the inner regions of all quasars is essentially the same, involving a compact, partially opaque core together with a beamed jet. Czerny et al. (2008) similarly find evidence for a blazar component in RQ QSOs by modeling their variability.

More sensitive empirical tests of whether the observed trend is due to substantial (but not directly detectable) absorption depressing the observed soft X-ray continuum at high luminosities, or to an increasing thermal fraction at lower luminosities could be performed by stacking counts in narrow energy bands from *Chandra* images of all QSOs (detected or not). Stacking has been used effectively this way in the CDFs (e.g., Steffen et al. 2007; Lehmer et al. 2007), but the task is more daunting for the ChaMP, where care must be taken to properly account for the effects of a much wider range of N_H^{Gal}, CCD quantum efficiency values, and exposure times.

A study of 35 Type 1 QSOs by Shemmer et al. (2008) finds that Γ increases (softens) with L/L_{Edd}, the latter derived from FWHM(Hβ) and νL_ν(5100 Å). Kelly et al. (2008) examine a larger sample, and find complicated relationships between M_{BH}, L_{UV}/L_{Edd}, and L_X/L_{Edd} that change direction depending on the emission line used to estimate M_{BH}. In a subsequent paper, we are extending our current analysis to include estimates for M_{BH} and L/L_{Edd} for the spectroscopic subsample of the current paper.

5.2. X-Ray Intrinsic Absorption Measurements

The quality of X-ray measurements of intrinsic absorbing columns depends strongly on the number of counts in the quasar, but also on the redshift of the object, as illustrated in a simple test in Figure 15.

Figure 16 shows our best-fit intrinsic absorption column measurements, which are overwhelmingly upper limits, either when assuming (as for counts less than 200) that $\Gamma = 1.9$ or when fitting both Γ and N_H^{intr} (for QSOs with more than 200 counts). Just one of the RL QSOs has detectable N_H^{intr}, which is nevertheless not large ($10^{21}\,\mathrm{cm}^{-2}$). Jet-related X-ray emission may reduce any absorption signatures.

Strong intrinsic absorption is relatively rare in RQ Type 1 QSOs. In the strictest interpretation of AGN unification models, none of these broad-line AGNs should be significantly X-ray-absorbed. Small obscured fractions might be expected by selection, which requires that the broad-line region (BLR) not be heavily dust-reddened, i.e. our view of the BLR is unobscured. X-ray absorbed BLAGN have therefore sometimes been called "anomalous." The obscured fraction of BLAGN from the literature spans a wide variety of samples and analysis methods, but most define "obscured" as $N_H^{\mathrm{intr}} > 10^{22}\,\mathrm{cm}^{-2}$ and
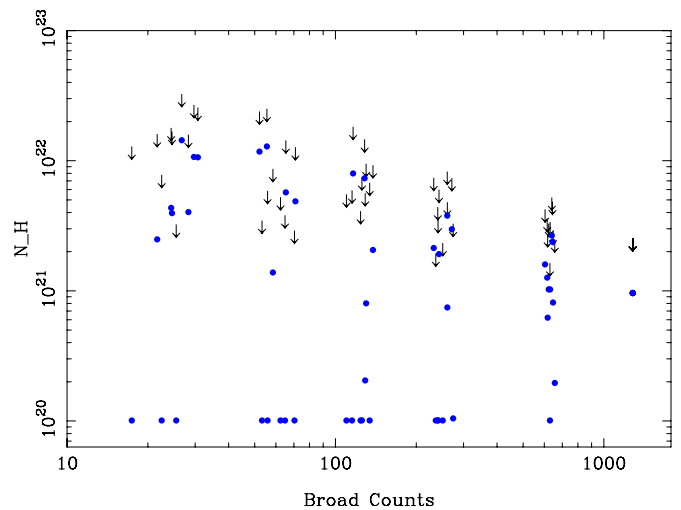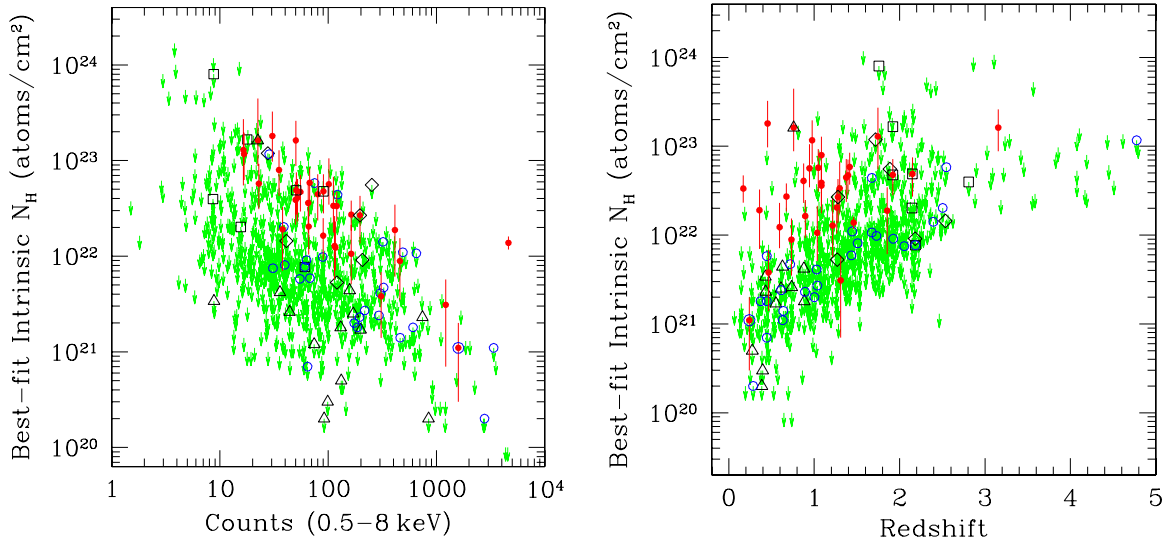

Figure 15. Best-fit log intrinsic absorption vs. (0.5–8 keV) counts for 10 random exposure-time subsamples scaled to achieve 2%, 5%, 10%, 20%, and 50% of the full original exposure time (100%, at the far right) for one bright X-ray source observed by *Chandra*. Best-fit values of N_H^{intr} are shown as blue dots, with the corresponding 90% upper confidence limit shown as black arrows. This plot shows a clear trend, reflecting the skewed (one-sided positive definite and logarithmic) nature of the N_H^{intr} parameter.

(A color version of this figure is available in the online journal.)

find fractions of about 10% or less (Perola et al. 2004; Page 2006; Mainieri et al. 2007). By contrast, selecting optically unobscured AGNs only from optical/IR photometry, and using X-ray HRs from *XMM*, Tajer et al. (2007) find 30%.

To estimate the obscured fraction of SDSS QSOs from the ChaMP, we first limit to the D2L sample and $z < 2$ to maximize the fraction that are X-ray detected (see Figure 9). We further limit to QSO-like optical luminosities $\log l_{2500\,\text{Å}} > 29.8$, yielding 630 QSOs, for which 498 (79%) are X-ray detections. If we rather stringently require that the 90% lower bound to the best-fit $\log N_H^{\mathrm{intr}}$ exceeds 22, then 50 of the 498 (10%) of X-ray detected QSOs are obscured. If instead we simply use the best-fit N_H^{intr}, 98 of 498 (20%) of detected QSOs are obscured. However, if we make the unlikely assumption that all X-ray-undetected QSOs are missed due to heavy intrinsic absorption, the obscured fraction could be as high as 29% and 36% for these two different methods, respectively.

We note that the correlation of dust to total column of X-ray absorbing metals is not strict. For instance, we know that a significant fraction of optically selected QSOs (13–20%; Reichard et al. 2003; Hewett & Foltz 2003; Knigge et al. 2008) appear as BAL QSOs, which are thought to be seen along a sightline piercing warm (ionized) absorbers. BAL QSOs are highly absorbed in X-rays (Green et al. 1995, 1996, 2001; Gallagher et al. 2002). All the BAL QSOs here have N_H^{intr} detections or upper limits that are greater than $3 \times 10^{22}\,\mathrm{cm}^{-2}$. An even larger fraction may harbor undetected warm absorbing material that is too smooth in its velocity and/or geometric distribution to show distinct absorbing troughs (Gierliński & Done 2004; Green et al. 2006). The frequency of warm X-ray absorbers has been shown to be about 50% (Porquet et al. 2004) in low-redshift (PG) QSOs. Again, the bias of (color-plus broad-line-based) optical selection decreases their number here. The fraction of detectably large N_H^{intr} in the fully X-ray-selected ChaMP is larger, but nearly all such examples are found in objects which appear optically as narrow-line AGN or absorption line galaxies (XBONGs), as shown by Silverman et al. (2005a).

Figure 16. Left: best-fit intrinsic absorption vs. (0.5–8 keV) counts for detected QSOs. Object type symbols are as described in Figure 3. The green arrows indicate upper limits, while detections (where the 90% lower limit exceeds log $N_H^{intr} = 20$) are red dots with 90% error bars. The strong decrease in the upper limit envelope traces the increased sensitivity as a function of detected counts. Only a handful of objects show significant absorption above 200 counts where simultaneous fits to Γ and N_H^{intr} are performed. Right: best-fit intrinsic absorption vs. redshift. The strong increase in the upper limit envelope reflects both the decrease in counts and the decreased sensitivity as a function of redshift, due to the rest-frame-absorbed region below $\sim$2 keV redshifting out of the *Chandra* bandpass.

(A color version of this figure is available in the online journal.)

6. X-RAY TO OPTICAL SEDs

Beyond the desire to know of real trends in the SEDs of QSOs for the sake of understanding accretion physics, such trends influence other scientifically important research. Corrections to derive bolometric luminosities (L_{bol}) from measured L_X depend strongly on SED trends. L_{bol} in turn is key to constraining such fundamental parameters as accretion efficiency and/or SMBH densities in the universe (e.g., Marconi et al. 2004), or active accretion lifetimes or duty cycles (e.g., Hopkins et al. 2005; Adelberger & Steidel 2005). As another example, to compare the AGN space densities found via optical versus X-ray selection, Silverman et al. (2005b, 2008) and others use the measured trend in α_{ox} to convert the X-ray luminosity function (LF) to an optical LF.

Numerous studies have debated the strength and origin of trends in the X-ray-to-optical luminosity ratio of optically selected quasars. This ratio is herein (and typically) characterized by the spectral slope α_{ox}. Most studies include large samples mixing both targeted and serendipitous X-ray observations (e.g., Avni & Tananbaum 1982; Wilkes et al. 1994; Vignali et al. 2003; Strateva et al. 2005; Steffen et al. 2006; Kelly et al. 2007a). All these studies, using widely varying techniques and sample compilations, have found a strong correlation between α_{ox} and optical luminosity, and several have also suggested a residual evolution of α_{ox} with redshift or lookback time, even after the luminosity correlation is accounted for.

While large sample sizes and appropriate statistical techniques (see Section 6.1) have been sought in these studies, the impact of sample selection effects combined with large intrinsic sample dispersions in luminosity may still dominate the observed correlations. These effects have been modeled and simulated by Yuan et al. (1998) and Tang et al. (2007) among others, who retrieve seemingly statistically significant but artificially induced correlations. They highlight the need for large, well-defined samples to alleviate this problem, and they also note the importance of minimizing the effects of a

strong L–z correlation induced by a single sample flux limit. The ChaMP/SDSS sample is a large step toward alleviating these problems.

Contamination by unrelated physical processes should be eliminated wherever feasible. As mentioned above, it is well-known that RL QSOs tend to be X-ray bright, and there is evidence that a distinct, jet-related physical process produces that extra X-ray emission. BAL QSOs, on the other hand, tend to be X-ray weak, because of intrinsic absorption from the warm (ionized) winds (Green et al. 2001; Gallagher et al. 2002). When investigating distributions and correlations amongst α_{ox}, l_o, and l_x, most previous authors have chosen to eliminate both BAL and RL QSOs to minimize contamination of (presumably) pure accretion-dominated X-ray emission. It is important to note that this precaution is neither complete, nor perhaps correct. For example, the intrinsic radio-loudness distribution of quasars does appear to be well modeled by a quasi-normal distribution with a 5% tail of RL objects (Cirasuolo et al. 2003), but the relationship of that distribution to X-ray emission is not well characterized. Even after removal of quasars with a radio/optical flux ratio above some limit, radio-related X-ray emission may pervade quasar samples, and affect the distributions we study. Similarly, the best quantitative measures of absorption profiles via, e.g., "balnicity" (Weymann et al. 1991) indicate that the fraction of quasars with intrinsic outflows may be significantly underestimated (Reichard et al. 2003), with classic BAL QSOs just the tip of the iceberg. Equally important may be that BALs to date are mainly detected only beyond $z \sim 1.4$ in ground-based optical spectroscopic quasar samples ($z \sim 1.5$ in SDSS spectra), so the low-redshift, low-luminosity end of the quasar distribution may harbor significant undetected warm absorption. We therefore examine a variety of subsamples within and without these classes. When we compare bivariate regression results $l_{2500 \text{Å}}$, $l_{2 \text{keV}}$, and α_{ox}, directly to Steffen et al. (2006; S06 hereafter), we follow their convention of excluding known RL QSOs and BAL QSOs, and expand somewhat to also eliminate QSOs with evident NALs, and NLS1s as well. We note that their

α_{ox} definition is the negative of the more conventional one we adopt here.

6.1. Statistical Tools and Methods

Many previous studies have emphasized the importance of including X-ray upper limits in the samples, which require appropriate statistical treatment using, e.g., survival analysis. Results from survival analysis can depend strongly on the number of detections, and therefore on the detection threshold, since in flux-limited samples, most detections are near that threshold. The *Chandra* fields used here span a wide range of effective exposure times, substantially alleviating the powerful effects that a single survey flux limit can have (e.g., by creating a very tight L_x–z correlation). Previous studies have managed to limit the fraction of upper limits by using mostly targeted X-ray observations (e.g., Wilkes et al. 1994), where exposure times are often chosen based on optical flux, or by judicious choice of subsamples (e.g., Strateva et al. 2005; Steffen et al. 2006) designed to fill the luminosity-redshift plane. For example, Strateva et al. (2005) uses SDSS spectroscopic AGNs from the SDSS Data Release 2 (DR2), observed by *ROSAT* PSPC for more than 11 ks. For this purpose, the DR2 AGN sample is already biased, since many spectroscopic targets are chosen as X-ray *ROSAT* or *FIRST* radio detections. Other AGNs they include to fill in the L–z plane were specifically targeted for *Chandra* or *XMM-Newton* observations for a variety of reasons. A slightly larger study by Steffen et al. (2006) added objects using mostly photometric AGN classifications and redshifts from COMBO-17, together with the Extended *Chandra* Deep Field (CDF) South (ECDF-S), but also several other small bright samples for the low L–z region. Even after selecting and combining various samples with high detection fractions, the use of Survival Analysis techniques to incorporate limits must sometimes be abandoned.[26] In summary, if significant selection biases may affect either the constituent subsamples or their ensemble, neither the inclusion of upper limits, nor the use of complex statistical analysis methods should convey the impression that statistical results are as robust as those from a uniform, complete, and well-characterized sample.

It is also worthwhile to consider the fact that some previous studies have appended low-luminosity subsamples (Seyferts 1s). Our SDSS sample excludes some of these objects because they would be spatially resolved. This may bias our sample in the sense that for low-redshift AGNs (e.g., 107 objects in the MainDet sample with $z \leqslant 0.55$) we include only those that are compact (optical light distribution consistent with the expected SDSS PSF). Most previous studies have instead attempted to include such objects, but then they correct for the inclusion of substantial host galaxy emission via, e.g., spectroscopic template fitting (Strateva et al. 2005). This may bias those samples in a different way by excluding the host contribution only for nearby objects.

6.1.1. Univariate Analyses

To compare two-sample distributions, we test the "null" hypothesis that two independent random samples subject to censoring (e.g., Γ for RL and RQ QSO) are randomly drawn from the same parent population. The programs for two-sample

tests that we use are the Gehan, or generalized Wilcoxon test, and the log-rank test in ASURV (Survival Analysis for Astronomy; LaValley et al. 1992). Again, we require $P_{max} < 0.05$ to call the distinction significant. For $P_{max} < 0.10$, we call the difference "marginal." The Kaplan–Meier method we employ to estimate the mean of a distribution allows for the inclusion of censored values (upper or lower limits).

6.1.2. Bivariate Regressions

Except where noted, all the correlations studied between X-ray and optical luminosity, and between α_{ox} and l_o are highly significant: $P < 10^{-4}$ by Cox Proportional Hazard, Kendall's τ, or Spearman's ρ tests, as implemented in the ASURV package (LaValley et al. 1992). We deem a correlation significant if the maximum probability P_{max} from all three tests is 0.05 or less. We perform bivariate linear regressions using the two-dimensional Kaplan–Meier (2KM) test (Schmitt 1985) as implemented in ASURV, which permits linear regression with limits in either axis.[27] We use 20 bootstrap iterations for error analysis, (more than sufficient given the large sample size here) and 20 bins in each axis, with origins 27.3 (23.0, 1.0) for $l_{2500\,\text{Å}}$ ($l_{2\,\text{keV}}$, α_{ox}), except where samples have been explicitly restricted in luminosity, or by object type to have $N < 200$, whereupon we use 10 bins.

For bivariate regressions between X-ray and optical luminosity, we make no assumptions about which luminosity constitutes the dependent or independent variable, and calculate the mean (bisector) of the ordinary least-squares (OLS) regression lines which minimize residuals for $Y(X)$, $X(Y)$, respectively.[28] While the intrinsic dependence of $\alpha_{ox}(l_o)$ or $\alpha_{ox}(l_x)$ is unknown, most studies assume α_{ox} to be the dependent variable, and quote slopes accordingly, so we will follow suit largely for purposes of comparison. We further caution that in samples with large dispersions, different regression methods can yield different results (see a recent mathematical review of related issues by Kelly 2007b).

For completeness, we provide statistical results in table format for a variety of subsamples which may be of interest, even beyond those discussed in the text. For ease of reference, tables listing bivariate statistical results (Tables 5–7) list samples in the same order as the table defining samples (Table 1).

6.2. α_{ox} for QSO Subsamples

Here we use the high detection fraction (D2L) sample, with high detection fraction, to examine the α_{ox} distributions of several subsamples, including targets. The mean α_{ox} for 1269 QSOs in the D2L sample is 1.429 ± 0.005 with median 1.370. Means and medians for the D2L sample and for subsamples discussed in this section are listed in Table 4, as are result for two-sample tests.

For 31 RL QSOs in the D2L sample, the mean $\alpha_{ox} = 1.377 \pm 0.028$ with median 1.392. Using the two-sample tests described in Section 6.1.1 above, this distribution is only marginally different than for the 1238 non-RL QSOs in the D2L sample. RL QSOs are thought to be more X-ray loud than RQ QSOs.

For the 23 known BAL QSOs in the D2L sample, the mean α_{ox} is 1.717 ± 0.028 with median 1.66, and the

---

[26] For example, Steffen et al. (2006) simply drop the X-ray limits when regressing with $l_{2\,\text{keV}}$ as the independent variable. We choose instead to incorporate the limits using the two-dimensional Kaplan–Meier (2KM) test (Schmitt 1985).

[27] Our results from the other two bivariate regression algorithms in ASURV (the Buckley–James method and the parametric EM Algorithm) are quite consistent.

[28] In the absence of limits, these results reduce reliably to the bisectors found by the SLOPES program (Feigelson & Babu 1992; Babu & Feigelson 1992; Isobe et al. 1990).

Table 6
Quasar Sample Bivariate Regression Results: $l_{2\,\mathrm{keV}}(l_{2500\,\text{Å}})$ OLS Bisector

Sample	Slope	Error	Intercept	Error
		Primary Samples		
Main	1.1171	0.0170	−7.5929	0.6365
MainDet	0.9372	0.0266	−1.9178	0.8797
NoTDet	0.9719	0.0259	−2.9508	0.8418
D2L	1.1350	0.0209	−8.1162	0.6329
D2LNoRB	1.1667	0.0238	−9.0641	0.7199
hiLo	1.2976	0.0340	−13.1316	1.0356
		Other Samples		
NoRB	1.1502	0.0146	−8.5922	0.6125
NoRBDet	0.9359	0.0253	−1.8745	0.8903
zLxBox	0.8421	0.0173	1.0177	0.6695
LoBox	0.9907	0.0310	−3.5191	0.9357
zBox	1.6658	0.1125	−24.3936	3.4355
zBoxDet	1.4088	0.0803	−16.3512	2.4564
D2LSy1	1.2299	0.0504	−10.6975	1.4746
D2LNoTRB	1.1908	0.0196	−9.7838	0.5921
S06	0.72	0.01	4.53	0.69

Notes. Samples tested are arranged in the same order as in Table 1. OLS refers to the ordinary least-squares regression. S06 are results from Steffen et al. (2006) for comparison.

Table 7
Quasar Sample Bivariate Regression Results: $\alpha_{\mathrm{ox}}(l_{2500\,\text{Å}})$ OLS

Sample	Slope	Error	Intercept	Error
		Primary Samples		
Main	0.0598	0.0066	−0.2776	0.1988
MainDet	0.0826	0.0066	−1.0331	0.1978
NoTDet	0.0732	0.0089	−0.7496	0.2681
D2L	0.0610	0.0085	−0.3189	0.2580
D2LNoRB	0.0516	0.0078	−0.0358	0.2377
hiLo	0.1284	0.0070	−2.3754	0.2151
		Other Samples		
NoRB	0.0513	0.0073	−0.0239	0.2217
NoRBDet	0.0804	0.0085	−0.9667	0.2546
D2LNoTRB	0.0482	0.0104	0.0652	0.3146
zLxBox	0.1943	0.0067	−4.4484	0.2033
LoBox	0.1895	0.0105	−4.2956	0.3176
zBox	0.1019	0.0242	−1.5709	0.7404
zBoxDet	0.1119	0.0267	−1.9335	0.8172
D2LSy1	0.0058	0.0175	1.3253	0.5160
S06	0.137	0.008	−2.638	0.240

Notes. Samples tested are arranged in the same order as in Table 1. OLS refers to the ordinary least-squares regression. S06 are results from Steffen et al. (2006) for comparison.

distribution is significantly different than for the non-BAL the D2L sample. The apparent X-ray weakness has been shown to be consistent with intrinsic absorption of a normal underlying X-ray continuum (Green et al. 2001; Gallagher et al. 2002).

For the eight known NALs in the D2L sample, the mean α_{ox} is 1.463 ± 0.056 with median 1.5, but the poor statistics render the distribution indistinguishable from the overall D2L sample.

For the 19 known NLS1s in the D2L sample, the mean α_{ox} is 1.54 ± 0.08 with median 1.43, again indistinguishable from the overall D2L sample.

6.3. X-Ray Luminosity $l_{2\,\mathrm{keV}}$ Versus Optical $l_{2500\,\text{Å}}$

Figure 17 shows a highly significant correlation of $l_{2\,\mathrm{keV}}$ with $l_{2500\,\text{Å}}$, and plots our best-fit regression lines. The bisector regression relationship for the SDSS/ChAMP sample (the Main sample, limits included, 2308 QSOs), is

$$\log(l_{2\,\mathrm{keV}}) = (1.117 \pm 0.017)\log(l_{2500\,\text{Å}}) - (7.59 \pm 0.64).$$

This slope is close to linear, and significantly different than the bisector slope $\beta = 0.72 \pm 0.01$ derived by S06 from their smaller, more diverse sample. The subsample philosophically closest to that of S06 is the NoRB sample, or its high detection fraction version the D2LNoRB sample, since they exclude known RL and BAL QSOs (as well as NALs and NLS2s), but include targets. The D2LNoRB sample bisector slope is $\beta = 1.115 \pm 0.015$. Our bisector slope results in Table 6 are closer to linear than S06 for all samples tested across the full luminosity range, including those that omit limits altogether. Figure 18 shows the MainDet sample (detections only) across a smaller luminosity range, to highlight the different QSO types.

A nearly linear result was also found by Hasinger (2005) for a sample of Type 1 QSOs that spanned a similarly large range of luminosities as our own. That work used an X-ray-selected sample with a high (∼ 95%) completeness for spectroscopic identifications, and concluded that the non-linear trends seen in optically selected samples probably result from selection effects.
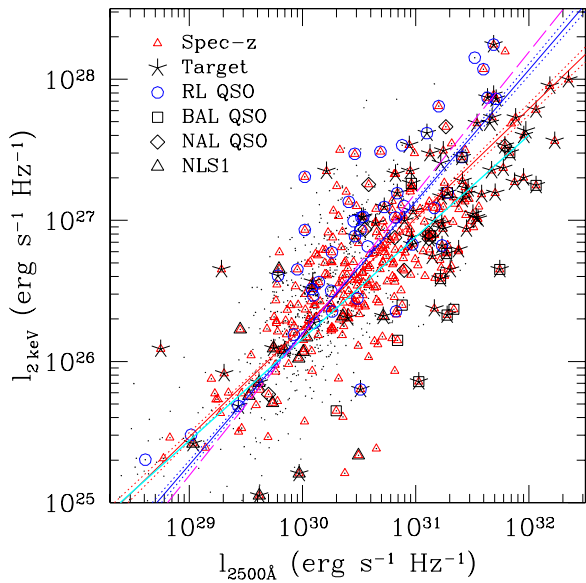

Figure 17. X-ray (2 keV) vs. optical (2500 Å) luminosity for the the Main sample. See Figure 3 for symbol types. The long-dashed magenta line is of slope unity, normalized to the sample means. The flattest fit is the best-fit (OLS bisector) relation from Steffen et al. (2006) (their Equation 1c), shown as a solid cyan line, spanning the luminosity range of their compilation. The best-fit OLS bisector regression line to the SDSS/ChAMP in the Main sample (including nondetections) is shown in blue, spanning the full plot. The short-dashed lines plotted using 1σ statistical errors to the ChAMP fits are so close to the best fit as to be barely discernible on the plot. The red line is a $Y(X)$ regression on the same data, illustrating the sensitivity of fits to regression method in high dispersion data.

(A color version of this figure is available in the online journal.)

6.4. α_{ox} Versus Optical Luminosity

Figure 19 (left) shows the trend of α_{ox} with $l_{2500\,\text{Å}}$ for the Main sample. While the detected QSOs appear as a large "blob," this is due to a combination of the SDSS depth, the QSO optical luminosity function, and the highly efficient QSO selection in the corresponding redshift range $1 < z < 2.5$ (see Figure 8). There is a highly significant correlation: $P < 10^{-4}$ by Cox Proportional Hazard, Kendall's τ, or Spearman's ρ for any of

Figure 18. Zoom-in of the X-ray (2 keV) vs. optical (2500 Å) luminosity plot for the MainDet sample. See Figure 3 for symbol types. Here we show a smaller luminosity range, and omit limits to highlight the classes indicated in the key. RL QSOs clearly populate the upper end of the distribution in X-ray luminosity, while BAL QSOs are underluminous in X-rays. The fits shown here are performed on the MainDet sample with detections only. Line types are the same as in Figure 17.

(A color version of this figure is available in the online journal.)

the samples considered (with or without limits). Our best-fit regression line minimizing residuals only in α_{ox} (e.g., a $Y(X)$ regression) for the Main sample is

$$\alpha_{ox} = (0.061 \pm 0.009) \log(l_{2500\,\text{Å}}) - (0.319 \pm 0.258).$$

This is significantly flatter than the results of S06 (0.137 ± 0.008), consistent with the more closely linear relationship we find above between X-ray and optical luminosity. As can be seen from Figure 19 (right) and Table 7, keeping targets but removing RL and BAL QSOs (the D2LNoRB sample) yields similarly flat slopes.

The classical Seyfert 1/QSO dividing line at $M_B \sim -23$ corresponds here to $\log(l_{2500\,\text{Å}}) \sim 29.8$ (*or* $\log(\nu_{2500}l_{2500\,\text{Å}}) \sim 44.9$). While this conventional partition is essentially arbitrary, it does represent a sharp discontinuity in the luminosity histogram of the current sample: six times as many objects have "QSO-like" optical luminosity as "Seyfert-like." The hiLo sample, restricted to luminous QSOs as above, yields a slope for the $\alpha_{ox}(l_{2500\,\text{Å}})$ relation of 0.128 ± 0.007, most similar to S06 and previous work. The SDSS/ChaMP sample does boast a larger number of low optical luminosity objects than most previous analyses, in large part because of the sensitivity of the *Chandra* observations, and these lower luminosity objects may be responsible in part for our different results across the full $l_{2500\,\text{Å}}$ range. Analysis of the (much smaller, with $N_{det} = 176$ and $N_{tot} = 260$) the D2LSy1 sample with Seyfert-like luminosities, suggests that no significant correlation exists ($P > 0.6$ for all tests). This highlights that the trend of $\alpha_{ox}(l_{2500\,\text{Å}})$ may not be linear, as also found by S06 and Kelly et al. (2007a), or may only apply for high luminosities.

Note that we have investigated whether the details of our luminosity and α_{ox} calculations affect the results. No significantly different scientific conclusions result from our use of best-fit Γ (which affects the X-ray K-correction) to calculate the X-ray

luminosity. For example, the MainDet sample $\alpha_{ox}(l_o)$ regression that results from instead using fixed $\Gamma = 1.9$ and best-fit N_H^{intr} has slope 0.077 and intercept -0.872.

Inasmuch as α_{ox} probes intrinsic accretion processes, it probably samples the balance between optical/UV blackbody thermal emission from a geometrically thin but optically thick accretion disk, against X-ray emission from a hot, optically thin corona that upscatters the seed UV photons from the disk. Various physical models can explain an $\alpha_{ox}-l_{2500}$Å correlation with plausible parameters, e.g., a disk truncation radius that increases with luminosity (Sobolewska et al. 2004). We also know that α_{ox} measurements can be affected by intrinsic absorption. This is proven by the extreme example of the BAL QSOs here and elsewhere (Green et al. 2001; Gallagher et al. 2002). Further evidence may come from a recent sample of AGN host galaxies of five clusters observed by *Chandra* and the Advanced Camera for Surveys (ACS) onboard *HST*, where Martel et al. (2007) found that the X-ray-to-optical flux ratio of the AGNs correlates with the inclination angle of the host galaxies[29]. If the observed trends are not dominated by selection effects (e.g., Tang et al. 2007), it seems likely that intrinsic absorption acts to increase the dispersion of an intrinsic relationship which is dominated by accretion physics.

7. EVOLUTION OF α_{OX}

In a sample with a strong $\alpha_{ox}(l_{2500\,\text{Å}})$ correlation, α_{ox} will naturally correlate strongly with redshift as well, due to the powerful redshift–luminosity trend shown in Figure 6. To determine whether any redshift evolution of α_{ox} occurs independent of its luminosity dependence, we use two methods.

First, we examine a subsample with a narrow range in $l_{2500\,\text{Å}}$ but a reasonably broad range in redshift. The zBox sample (Table 7) contains all the MainDet sample objects with $30.25 < \log(l_{2500\,\text{Å}}) < 31$ and $0.5 < z < 2.5$. This sample shows no significant correlation between α_{ox} and redshift ($P_{max} = 19\%$). Accordingly, the nominal best-fit regression has a slope consistent with zero (-0.001 ± 0.014).

Next, we can subtract the best-fit $\alpha_{ox}(l_{2500\,\text{Å}})$ regression to the more luminous hiLo sample ($\log(l_{2500\,\text{Å}}) > 29.8$), where a simple linear fit seems applicable, and look for any residual $\alpha_{ox}(z)$ dependence (evolution). The expected $\alpha_{ox}(z)$ trend is significant for the hiLo sample, induced by the $\alpha_{ox}(l_{2500\,\text{Å}})$ and $l_{2500\,\text{Å}}(z)$ relationships. We then subtract the best-fit regression trend from Table 7. The residual $\Delta\alpha_{ox}$ shows no trend with redshift in Figure 20 (bottom) or in correlation tests ($P_{max} = 0.80$).

The large subsample sizes afforded by the SDSS/ChaMP QSO sample allow us to conclude, without resort to more elaborate statistical analyses, that any apparent evolutionary trend can be accounted for by the $l_{2500\,\text{Å}}(z)$ correlation in our sample, and that such evolution is at best very weak in the range $0.5 < z < 2.5$.

7.1. α_{ox} Versus X-ray Luminosity

A weaker trend has also been noted in the correlation between α_{ox} and $l_{2\,keV}$ (Green et al. 1995; Steffen et al. 2006). For the Main sample, we find

$$\alpha_{ox} = (0.003 \pm 0.010) \log(l_{2\,keV}) + (1.384 \pm 0.261)$$

---

[29] The X-ray/optical versus inclination correlation holds for late- but not early-type galaxies, so may not apply directly to Type 1 QSOs if they are mostly in elliptical hosts.
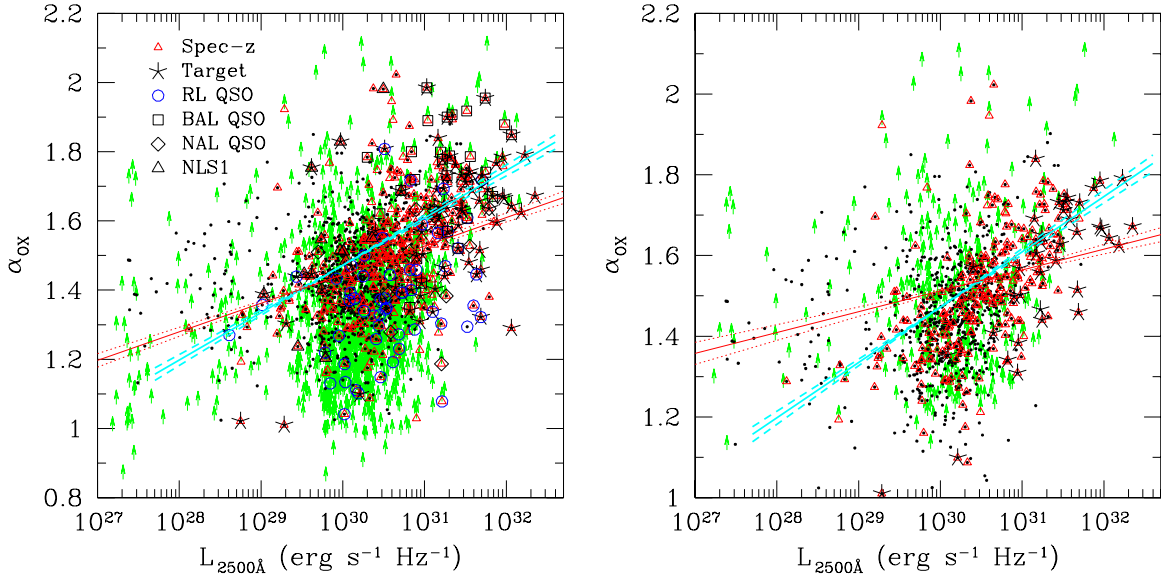
Figure 19. α_{ox} vs. optical 2500 Å log luminosity for the Main sample (left) and the D2LNoRB sample (right). See Figure 3 for symbol types. The best-fit OLS $Y(X)$ regression for each ChaMP sample is shown as a red line with errors. The best-fit relation from Steffen et al. (2006) is shown as a solid cyan line.

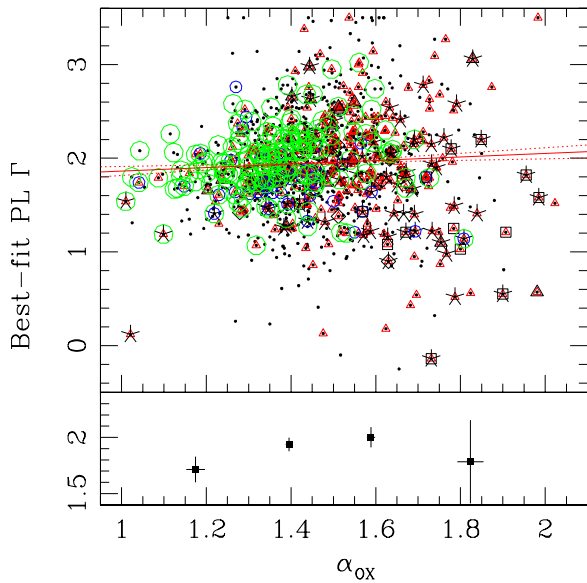(A color version of this figure is available in the online journal.)
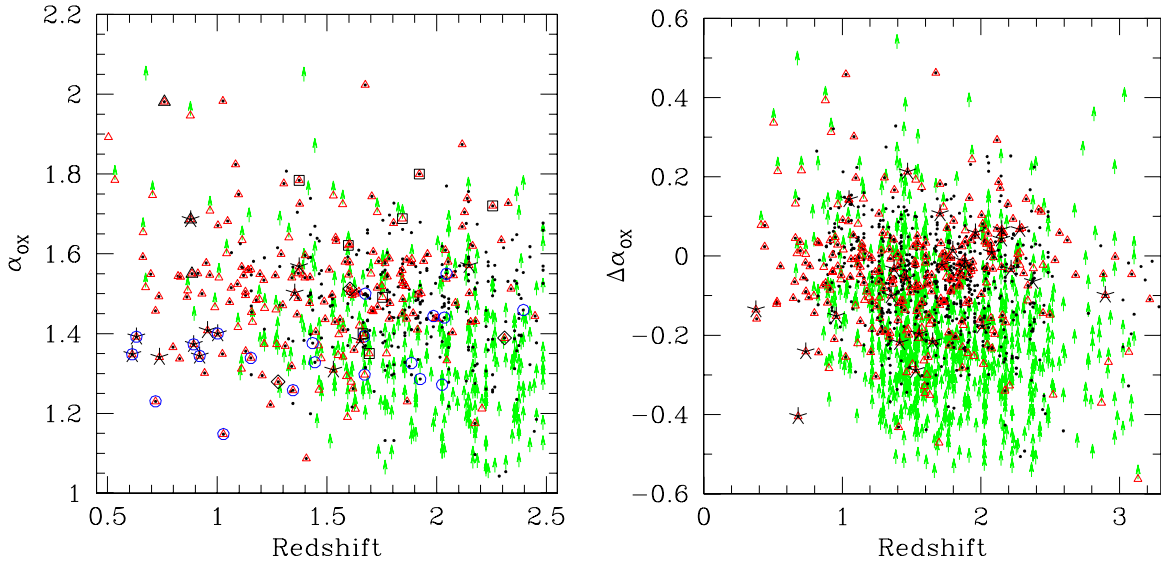
Figure 20. Top: α_{ox} vs. redshift for the zBox sample, restricted in log $l_{2500\,\text{Å}}$ to the range 30.25–31. No significant trend exists. See Figure 3 for symbol types. Bottom: $\Delta\alpha_{ox}$ vs. redshift for the hiLo sample (log $(l_{2500\,\text{Å}} > 29.8)$ after subtraction of its best-fit $\alpha_{ox}(l_{2500\,\text{Å}})$ relation in Table 7. Although the redshift range remains wide for this subsample, no trend is apparent.

(A color version of this figure is available in the online journal.)

which (while the correlation is significant) is consistent with zero slope. With a higher detection fraction, the the D2L sample yields slope -0.0280 ± 0.0087, so that objects more luminous in X-rays are also X-ray brighter (relative to $l_{2500\,\text{Å}}$). Further removing RL and BAL QSOs (the D2LNoRB sample) does not change the best-fit parameters. While the effects of different samples on the measured regression is significant, the $\alpha_{ox}(l_{2\,\text{keV}})$ relationship is particularly affected by limits, since they affect both axes.

An apparent luminosity dependence of α_{ox} is generated artificially if the intrinsic dispersion in optical luminosity σ_o exceeds that for X-rays σ_x (Yuan et al. 1998; Tang et al. 2007).[30]

The significance of the induced correlation is proportional to $\sigma_o^2/\Delta l_o^2$ where Δl_o is the optical/UV luminosity range of the sample. The magnitude of the biases also depends on the luminosity function and sample flux limits. Given these effects, the apparently strong correlations so far published are all consistent with no intrinsic dependence (Tang et al. 2007). The most convincing remedy is likely to be a volume-limited sample that spans a large range of both redshift and luminosity with high detection fraction. This requires careful treatment of large combined samples, similar to Silverman et al. (2005b, 2008), including detailed pixel-by-pixel flux (and consequently volume) limits. While the groundwork has been laid by the ChaMP's `xskycover` analysis, such a project is well beyond the scope of this paper.

---

[30] Any correlation between a dependent variable B which is derived via $B \propto A^{-1}$ from an independent variable A will be similarly affected in samples with large dispersion.

Figure 21. Top: best-fit X-ray spectral power-law slope Γ vs. α_{ox} for the MainDet sample. The best-fit OLS regression relation for this sample is shown with a red line, and associated errors in dashed lines. The large open green circles show QSOs with more than 200 (0.5–8 keV) counts and simultaneous Γ–N_H^{intr} fits. See Figure 3 for other symbol types. Bottom: mean Γ values are shown at the mean redshift for QSOs in four redshift bins of width $\Delta\alpha_{ox} = 0.25$ for the MainDet sample. Error bars show the error in the means for both axes.

(A color version of this figure is available in the online journal.)

7.2. α_{ox} Versus Γ

Figure 21 shows best-fit Γ plotted against α_{ox} for the MainDet sample. We detect for the first time a significant but shallow correlation between Γ and α_{ox}. Quasars that are relatively X-ray weak (larger α_{ox}) tend to have softer continuum slopes (larger Γ). Figure 21 shows the best-fit regression relation for the MainDet sample,

$$\Gamma = (0.188 \pm 0.106)\,\alpha_{ox} + (1.676 \pm 0.153).$$

The measured slope of the correlation is likely somewhat suppressed by the warm absorbers commonly found even in Type 1 AGNs. In Figure 21, for the hard/weak region bounded by $\alpha_{ox} > 1.6$ and $\Gamma < 1$, we find a BAL (indicated by open black squares) is visible for every object for which a spectrum exists covering blueward of rest-frame CIV $\lambda1550$. It is likely that most if not all objects in this region are BALs, as could be determined, e.g., from rest-frame UV spectroscopy. Again, these objects are probably not intrinsically flat, but rather have a hard best-fit Γ due to undetected intrinsic absorption.

Other samples shown in Table 8 omit targets, and RL or possibly absorbed QSOs all show steeper slopes. The steepest slope shown is for the HiCtNoTRB sample, which also includes only objects with counts greater than 200, where N_H^{intr} is fitted independently of Γ. This further supports that absorption if anything flattens the apparent relation compared to the intrinsic relation.

8. DISCUSSION

In this study, we have presented the largest homogeneous study to date of optically selected broad-line quasars (from the SDSS) with sensitive X-ray flux limits (from *Chandra*; mode 2×10^{-14} erg cm^{-2} s^{-1}; 0.5–8 keV). Our large sample highlights the large dispersion in quasar properties that is

Table 8
Quasar Sample Bivariate Regression Results: $\Gamma(\alpha_{ox})$ OLS

Sample	Slope	Error	Intercept	Error
MainDet	0.188	0.106	1.676	0.153
NoTDet	0.274	0.108	1.566	0.154
NoRBDet	0.340	0.109	1.466	0.154
HiCt	0.342	0.202	1.507	0.259
HiCtNoTRB	0.358	0.179	1.529	0.225

Notes. Samples tested are arranged in the same order as in Table 1. OLS refers to the ordinary least-squares regression.

unveiled whenever sensitive limits and wide sky areas are combined.

We confirm and extend several well-known multiwavelength relations. The relationship between α_{ox} and 2500 Å luminosity is confirmed for high luminosities ($M_B \lesssim -23$, or $\log(l_{2500\,\text{Å}}) \gtrsim 29.8(\log(\nu_{2500}l_{2500\,\text{Å}}) \gtrsim 44.9)$ with slopes similar to those found previously (e.g., S06). Including a wider luminosity range inevitably produces a flatter relation across a range of subsamples which test the effects of excluding *Chandra* PI targets, RL QSOs, and QSOs with BALs, or NALs as well as NLS1s. No significant $\alpha_{ox}(l_{2500\,\text{Å}})$ correlation exists for objects (68% detected) at lower luminosities. Another possibility is that the relation simply flattens at low luminosities, or has a higher-order luminosity dependence (e.g., Kelly et al. 2007a).

We find for the first time a significant, robust and rather steep dependence of X-ray continuum slope Γ on X-ray luminosity $l_{2\,\text{keV}}$ in the sense that the spectrum hardens with increasing $l_{2\,\text{keV}}$. A trend in the opposite sense has been reported recently for AGNs in the *Chandra* Deep Fields (Saez 2008), but may be dominated by differences between Type 1 and Type 2 AGNs.

We also report a shallow but significant trend that Γ is harder for relatively X-ray bright (low α_{ox}) QSOs. We note that X-ray bright QSOs include the RL QSOs, and that RL QSOs also have predominantly flatter (harder) Γ. We thus speculate that the overall trends of $\Gamma(\alpha_{ox})$ and $\Gamma(l_{2\,\text{keV}})$ both reflect an increase in the nonthermal emission fraction toward higher X-ray luminosities. Not all QSOs with a strong nonthermal X-ray emission component are necessarily radio loud-detectable radio loudness may pertain only to a fraction of these objects. Radio bright phases may be short compared to the overall QSO lifetime and/or episodic.

The black hole masses in AGNs are 5–8 orders of magnitude larger than those in Galactic black hole (GBH) X-ray binaries. Since for a given L/L_{Edd} the disc temperature scales with mass as $M^{-1/4}$, AGN disks are cooler than in GBHs. The thermal accretion disk emission component that dominates the soft X-ray emission ($\sim 2\,\text{keV}$) in GBHs corresponds to optical/UV (~ 2500 Å) emission in AGNs. Similarly, the nonthermal emission (probably from Comptonized emission from the disk's corona) sampled as X-ray emission in AGNs comes from harder ($\sim 20\,\text{keV}$) X-rays in GBHs. Type 1 QSOs may be analogous to GBH binaries in the high/soft state (Sobolewska et al. 2008) where a similar trend is seen in Γ versus a disc/Comptonization index α_{GBH} (analogous to α_{ox} for QSOs) as we report here. Jester et al. (2006) also compare the disk versus nonthermal emission fraction of GBHs and AGNs, and find that AGNs segregate by radio loudness similarly to GBHs in regions where luminosity and/or nonthermal fraction are high. While the correlations we

find lend significant support to these interpretations, the scatter is large, and could be significantly reduced if extrinsic effects can be identified and corrected for.

To better understand the intrinsic physics of accretion requires identifying and quantifying extrinsic effects such as absorption and nonthermal processes. Absorption may occur close to the SMBH gravitational radius, in the BLR, a molecular torus, surrounding star-forming regions, the outer host galaxy, or at intervening redshifts. The intrinsic absorption may be orientation-dependent, may evolve with redshift, and may be a function of luminosity as well. Contributions from nonthermal processes certainly play a role, whether or not it is reflected in detectable radio emission, and that role may change with SMBH mass, spin, and environment, so consequently with look-back time as well.

Let us face it—quasars are complicated, but on average they do not change much. If quasar SED changes with luminosity were large compared to the dispersion in the population and relatively immune to selection effects, we would have been using them for standard candles a long time ago. Large samples, uniformly observed and analyzed, offer the greatest hope to disentangle the intertwining mysteries.

APPENDIX

The ChaMP has developed and implemented an `xskycover` pipeline which creates sensitivity maps for all ChaMP sky regions imaged by ACIS. This allows (1) identification of imaged-but-undetected objects, (2) counts limits for 50% and 90% detection completeness, (3) flux sensitivity versus sky coverage for any subset of obsids, necessary for log N–log S and luminosity function calculations, and (4) flux upper limits at any sky position. The basic recipe is as follows. We use the `wavdetect` detection algorithm in CIAO (Freeman et al. 2002) to generate threshold maps at each `wavdetect` kernel scale actually run (1, 2, 4, 8, 16, and 32 pixels). The threshold maps, computed from the local background intensity, determine the magnitude of the source counts necessary for a detection at each pixel with a detection threshold of $P = 10^{-6}$ (corresponding to 1 false source per 10^6 pixels). Thus, when a source is *not* detected at a given location, the threshold map value serves as an upper limit to the source counts. Nominally, a source with true intensity equal to this counts limit would be detected in approximately half the instances that the source is observed under the same conditions. To retain fidelity yet create a reasonably sized and easily sampled sensitivity table covering the full ChaMP, we first average the threshold map values in sky pixels, each 10×10 arcsec, whose boundaries are chosen to match a regular commensurate grid across the sky. The final value of this counts limit in any given sky pixel is interpolated from the two threshold maps computed at wavelet scales that bracket the size of the PSF at that location.[31]

Note that the identification of the threshold map value one-to-one with the counts limit is valid only for a specific shape of the PSF (see Equation (6) of Freeman et al. 2002). In particular, the strength of the putative source can vary widely based on the correspondence between the PSF size and the wavelet scale, as well as the shape of the PSF. For non-Gaussian PSF shapes (such as are found with *Chandra* at larger OAAs), the threshold values must be corrected before a source counts limit is determined. We calibrate this correction factor by comparing the detection threshold map values with simulated source-retrieval experiments conducted on a subsample of ChaMP fields—the 130 Cycle 1–2 obsids studied by Kim et al. (2007a). While the threshold values give us a reliable map of variation on the sky, we must find a normalization from these simulations. Summing over a large number ($\sim 50{,}000$) of simulated sources, we compare the actual detection fraction from the simulations to the ratio of input (simulated) counts to derived (threshold) counts. From the fine binning available in these data, we interpolate to find the normalization that yields the correct counts values for 50% and 90% completeness, across a range of exposures, background levels, chip types, and OAAs. Our experiments show that the only significant dependence of the correction factor (normalization) is on OAA, and that dependence warrants only a linear correction dependence with best fit $N_{50} = 1.32 + 0.198 \times \mathrm{OAA}$ ($N_{90} = 2.08 + 0.331 \times \mathrm{OAA}$) for 50% (90%) source detection probability.

Our method has been verified recently by Aldcroft et al. (2008) using the CDF-S data available from the CXC. These data include the full 1.8 Msec from 2000 (Giacconi et al. 2002), and Director's Discretionary Time observations in 2007. The full

---

[31] The 39% radius is determined using the PSF enclosed counts fraction, which corresponds to the 1σ two-dimensional PSF size, from the library generated by the *Chandra* X-Ray Center (CXC) Calibration Group as documented at http://cxc.harvard.edu/cal/Hrma/psf.

1.8 Msec exposure was used to generate a source list which extended to faint fluxes. The 21 individual obsids comprising the full exposure were then treated as realizations of an experiment to detect these sources and the ensemble of detection statistics were analyzed by the same method as used for the ~50,000 simulated sources. We found excellent agreement for the 50% detection threshold and a slight disparity (10%) for the 90% detection threshold which could be explained by source variability.

REFERENCES

Adelberger, K. L., & Steidel, C. C., ApJ, 629, 636
Aldcroft, T. L. 2006, Bull. Am. Astron. Soc., 38, 376
Aldcroft, T. L., Green, P. J., Connelly, J., Kashyap, V., & Kim, D.-W. 2008, Bull. Am. Astron. Soc., 40, in press
Antonucci, R. 1993, ARA&A, 31, 473
Avni, Y., & Tananbaum, H. 1982, ApJ, 262, L17
Babu, G. J., & Feigelson, E. D. 1992, Simul. Comput., 21, 533
Ballantyne, D. R., Everett, J. E., & Murray, N. 2006, ApJ, 639, 740
Barger, A. J., Cowie, L. L., Mushotzky, R. F., Yang, Y., Wang, W.-H., Steffen, A. T., & Capak, P. 2005, AJ, 129, 578
Barvainis, R., Lehár, J., Birkinshaw, M., Falcke, H., & Blundell, K. M. 2005, ApJ, 618, 108
Becker, R. H., White, R. L., & Helfand, D. J. 1995, ApJ, 450, 559
Blackburne, J. A., Pooley, D., & Rappaport, S. 2006, ApJ, 640, 569
Blundell, K. M., & Beasley, A. J. 1998, MNRAS, 299, 165
Boller, T., Brandt, W. N., & Fink, H. 1996, A&A, 305, 53
Boroson, T. A. 2002, ApJ, 565, 78
Boroson, T. A., & Green, R. F. 1992, ApJS, 80, 109
Boyle, B. J., Shanks, T., & Peterson, B. A. 1988, MNRAS, 235, 935
Brandt, W. N., & Hasinger, G. 2005, ARA&A, 43, 827
Cirasuolo, M., Celotti, A., Magliocchetti, M., & Danese, L. 2003, MNRAS, 346, 447
Condon, J. J., Cotton, W. D., Greisen, E. W., Yin, Q. F., Perley, R. A., Taylor, G. B., & Broderick, J. J. 1998, AJ, 115, 1693
Croom, S. M., Smith, R. J., Boyle, B. J., Shanks, T., Miller, L., Outram, P. J., & Loaring, N. S. 2004, MNRAS, 349, 1397
Cash, W. 1979, ApJ, 228, 939
Czerny, B., Siemiginowska, A., Janiuk, A., & Gupta, A. C. 2008, MNRAS, 386, 1557
Dai, X., Chartas, G., Eracleous, M., & Garmire, G. P. 2004, ApJ, 605, 45
Dai, X., Shankar, F., & Sivakoff, G. R. 2008, ApJ, 672, 108
Dickey, J. M., & Lockman, F. J. 1990, ARA&A, 28, 215
Fabian, A. C., Iwasawa, K., Reynolds, C. S., & Young, A. J. 2000, PASP, 112, 1145
Fabbiano, G., et al. 2007, Astron. Data Anal. Softw. Syst. XVI, 376, 172
Falcke, H., Körding, E., & Markoff, S. 2004, A&Ap, 414, 895
Feigelson, E. D., & Babu, G. J. 1992, ApJ, 397, 55
Ferrarese, L., & Merritt, D. 2000, ApJ, 539, L9
Freeman, P. E., Kashyap, V., Rosner, R., & Lamb, D. Q. 2002, ApJS, 138, 185
Galbiati, E., et al. 2005, A&A, 430, 927
Gallagher, S. C., et al. 2002, ApJ, 567, 37
Gebhardt, K., et al. 2000, ApJ, 539, L13
Giacconi, R., et al. 2002, ApJS, 139, 369
Gierliński, M., & Done, C. 2004, MNRAS, 349, L7
Gilli, R., Comastri, A., & Hasinger, G. 2007, A&A, 463, 79
Granato, G. L., et al. 2004, ApJ, 600, 580
Green, P. J. 1996, ApJ, 467, 61
Green, P. J. 2006, ApJ, 644, 733
Green, P. J., Infante, L., Lopez, S., Aldcroft, T. L., & Winn, J. N. 2005, ApJ, 630, 142
Green, A. R., McHardy, I. M., & Lehto, H. J. 1993, MNRAS, 265, 664
Green, P. J., et al. 1995, ApJ, 450, 51
Green, P. J., et al. 2001, ApJ, 558, 109
Green, P. J., et al. 2002, ApJ, 571, 721
Green, P. J., et al. 2004, ApJS, 150, 43
Grindlay, J. E., et al. 2005, ApJ, 635, 920
Grupe, D., Wills, B. J., Leighly, K. M., & Meusinger, H. 2004, AJ, 127, 156
Hewett, P. C., & Foltz, G. B. 2003, AJ, 125, 1784
Hewett, P. C., Foltz, C. B., & Chaffee, F. H. 1995, AJ, 109, 1498
Hasinger, G. 2005, in Growing Black Holes: Accretion in a Cosmological Context, ed. A. Merloni, S. Nayakshin, & R. Sunyaev (Berlin: Springer)
Hennawi, J. F., et al. 2006, AJ, 131, 1

Hopkins, P. F., Hernquist, L., Cox, T. J., Di Matteo, T., Robertson, B., & Springel, V. 2006, ApJS, 163, 1
Hopkins, P. F., Hernquist, L., Cox, T. J., Di Matteo, T., Robertson, B., & Volker, S. 2005, ApJ, 630, 705
Hopkins, P. F., et al. 2008, ApJS, 175, 356
Isobe, T., Feigelson, E. D., Akritas, M., & Babu, G. J. 1990, ApJ, 364, 104
Ivezić, Ž., et al. 2002, AJ, 124, 2364
Jester, S., Körding, E., & Fender, R. 2006, VI Microquasar Workshop: Microquasars and Beyond
Jiang, L., Fan, X., Ivezić, Ž., Richards, G. T., Schneider, D. P., Strauss, M. A., & Kelly, B. C. 2007, ApJ, 656, 680
Just, D. W., Brandt, W. N., Shemmer, O., Steffen, A. T., Schneider, D. P., Chartas, G., & Garmire, G. P. 2007, ApJ, 665, 1004
Kelly, B. C. 2007, ApJ, 665, 1489
Kelly, B. C., Bechtold, J., Siemiginowska, A., Aldcroft, T., & Sobolewska, M. 2007, ApJ, 657, 116
Kelly, B. C., Bechtold, J., Trump, J. R., Vestergaard, M., & Siemiginowska, A. 2008, ApJS, 176, 355
Kim, D.-W., et al. 2004, ApJS, 150, 19
Kim, M., Wilkes, B. J., Kim, D.-W., Green, P. J., Barkhouse, W. A., Lee, M. G., Silverman, J. D., & Tananbaum, H. D. 2007a, ApJ, 659, 29
Kim, M., et al. 2007b, ApJS, 169, 401
Knigge, C., Scaringi, S., Goad, M. R., & Cottis, C. E. 2008, MNRAS, 386, 1426
La Franca, F., et al. 2005, ApJ, 635, 864
LaValley, M., Isobe, T., & Feigelson, E. D. 1992, ADASS, 1, 245
Lamer, G., Schwope, A., Wisotzki, L., & Christensen, L. 2006, A&A, 454, 493
Lehmer, B. D., et al. 2007, ApJ, 657, 681
Maccarone, T. J., Gallo, E., & Fender, R. 2003, MNRAS, 345, L19
Mainieri, V., et al. 2007, ApJS, 172, 368
Marconi, A., Risaliti, G., Gilli, R., Hunt, L. K., Maiolino, R., & Salvati, M. 2004, MNRAS, 351, 16
Martel, A. R., Menanteau, F., Tozzi, P., Ford, H. C., & Infante, L. 2007, ApJS, 168, 19
Middleton, M., Done, C., & Gierliński, M. 2007, MNRAS, 381, 1426
Misawa, T., Eracleous, M., Chartas, G., & Charlton, J. C. 2008, ApJ, 677, 863
Myers, A. D., et al. 2006, ApJ, 638, 622
Myers, A. D., et al. 2007, ApJ, 658, 99
Myers, A. D., et al. 2008, ApJ, 678, 635
Oke, J. B., & Gunn, J. E. 1983, ApJ, 266, 713
Osterbrock, D. E., & Pogge, R. W. 1985, ApJ, 297, 166
Page, C. G. 2006, Astron. Data Anal. Softw. Syst. XV, 351, 85
Page, K. L., Reeves, J. N., O'Brien, P. T., Turner, M. J. L., & Worrall, D. M. 2004, MNRAS, 353, 133
Perola, G. C., et al. 2004, A&A, 421, 491
Porquet, D., Reeves, J. N., O'Brien, P., & Brinkmann, W. 2004, A&A, 422, 85
Ptak, A., & Griffiths, R. 2003, Astron. Data Anal. Softw. Syst. XII, 295, 465
Reeves, J. N., & Turner, M. J. L. 2000, MNRAS, 316, 234
Reichard, T. A., et al. 2003, AJ, 126, 2594
Reynolds, C. S., & Nowak, M. A. 2003, Phys. Rep., 377, 389
Richards, G. T., et al. 2001, AJ, 121, 2308
Richards, G. T., et al. 2002, AJ, 123, 2945
Richards, G. T., et al. 2004, ApJS, 155, 257
Richards, G. T., et al. 2005, MNRAS, 360, 839
Richards, G. T., et al. 2006a, AJ, 131, 2766
Richards, G. T., et al. 2006b, ApJS, 166, 470
Richards, G. T., et al. 2008, ApJS, in press (arXiv:0809.3952R)
Saez, C., et al. 2008, AJ, 135, 1505
Scannapieco, E., Silk, J., & Bouwens, R. 2005, ApJ, 635, L13
Schmitt, J. H. 1985, ApJ, 293, 178
Schneider, D. P., Schmidt, M., & Gunn, J. E. 1994, AJ, 107, 1245
Schneider, D. P., et al. 2007, AJ, 134, 102
Shastri, P., Wilkes, B. J., Elvis, M., & McDowell, J. 1993, ApJ, 410, 29
Shemmer, O., Brandt, W. N., Netzer, H., Maiolino, R., & Kaspi, S. 2006, ApJ, 646, L29
Shemmer, O., Brandt, W. N., Netzer, H., Maiolino, R., & Kaspi, S. 2008, ApJ, 682, 81
Shen, S., White, S. D. M., Mo, H. J., Voges, W., Kauffmann, G., Tremonti, C., & Anderson, S. F. 2006, MNRAS, 369, 1639
Siemiginowska, A., Cheung, C. C., LaMassa, S., Burke, D. J., Aldcroft, T. L., Bechtold, J., Elvis, M., & Worrall, D. M. 2005, ApJ, 632, 110
Silverman, J. D., et al. 2005a, ApJ, 618, 123
Silverman, J. D., et al. 2005b, ApJ, 624, 630
Silverman, J. D., et al. 2008, ApJ, 679, 118
Sobolewska, M. A., Gierliński, M., & Siemiginowska, A. 2008, MNRAS, submitted
Sobolewska, M. A., Siemiginowska, A., & Zdotycki, P. T. 2004, ApJ, 617, 102

Steffen, A. T., Strateva, I., Brandt, W. N., Alexander, D. M., Koekemoer, A. M., Lehmer, B. D., Schneider, D. P., & Vignali, C. 2006, AJ, 131, 2826
Steffen, A. T., et al. 2007, ApJL, 667, L25
Strateva, I., Brandt, W. N., Alexander, D. M., Koekemoer, A. M., Lehmer, B. D., Schneider, D. P., & Vignali, C. 2006, AJ, 131, 2826
Strateva, I. V., Brandt, W. N., Schneider, D. P., Vanden Berk, D. G., & Vignali, C. 2005, AJ, 130, 387
Tajer, M., et al. 2007, A&A, 467, 73
Tang, S., Zhang, S. N., & Hopkins, P. F. 2007, MNRAS, 377, 1113
Treister, E., & Urry, C. M. 2006, ApJ, 652, L79
Trump, J. R., et al. 2006, ApJS, 165, 1
Ueda, Y., Akiyama, M., Ohta, K., & Takamitsu, M. 2003, ApJ, 598, 886
Vignali, C., Brandt, W. N., & Schneider, D. P. 2003, AJ, 125, 433
Vignali, C., Brandt, W. N., Schneider, D. P., & Kaspi, S. 2005, AJ, 129, 2519
Weinstein, M. A., et al. 2004, ApJS, 155, 243
Weymann, R. J., Morris, S. L., Foltz, C. B., & Hewett, P. C. 1991, ApJ, 373, 23

White, R. L., Helfand, D. J., Becker, R. H., Glikman, E., & de Vries, W. 2007, ApJ, 654, 99
Wilkes, B. J., Tananbaum, H., Worrall, D. M., Avni, Y., Oey, M. S., & Flanagan, J. 1994, ApJS, 92, 53
Williams, R. J., Mathur, S., & Pogge, R. W. 2004, ApJ, 610, 737
Wilman, R. J., & Fabian, A. C. 1999, ApJ, 522, 157
Wolf, C., Wisotzki, L., Borch, A., Dye, S., Kleinheinrich, M., & Meisenheimer, K. 2003, A&A, 408, 499
Worrall, D. M., Tananbaum, H., Giommi, P., & Zamorani, G. 1987, ApJ, 313, 596
Wyithe, J. S. B., & Loeb, A. 2002, ApJ, 581, 886
Wyithe, J. S. B., & Loeb, A. 2005, ApJ, 634, 910
York, D. G., et al. 2000, AJ, 120, 1579
Yu, Q., & Tremaine, S. 2002, MNRAS, 335, 965
Yuan, W., Brinkmann, W., Siebert, J., & Voges, W. 1998, A&A, 330, 108
Zamorani, G., et al. 1981, ApJ, 245, 357